CORE
Metadata, citation and similar papers at core.ac.uk
Provided by Institutional Research Information System University of Turin

PHYSICAL REVIEW D **91,** 112012 (2015)

Charged jet cross sections and properties in proton-proton collisions at $\sqrt{s} = 7$ TeV

B. Abelev *et al.*[*]
(ALICE Collaboration)

(Received 19 November 2014; published 22 June 2015)

The differential charged jet cross sections, jet fragmentation distributions, and jet shapes are measured in minimum bias proton-proton collisions at center-of-mass energy $\sqrt{s} = 7$ TeV using the ALICE detector at the LHC. Jets are reconstructed from charged particle momenta in the midrapidity region using the sequential recombination k_T and anti-k_T as well as the SISCone jet finding algorithms with several resolution parameters in the range $R = 0.2$–0.6. Differential jet production cross sections measured with the three jet finders are in agreement in the transverse momentum (p_T) interval $20 < p_T^{\mathrm{jet,ch}} < 100$ GeV/c. They are also consistent with prior measurements carried out at the LHC by the ATLAS Collaboration. The jet charged particle multiplicity rises monotonically with increasing jet p_T, in qualitative agreement with prior observations at lower energies. The transverse profiles of leading jets are investigated using radial momentum density distributions as well as distributions of the average radius containing 80% ($\langle R_{80} \rangle$) of the reconstructed jet p_T. The fragmentation of leading jets with $R = 0.4$ using scaled p_T spectra of the jet constituents is studied. The measurements are compared to model calculations from event generators (PYTHIA, PHOJET, HERWIG). The measured radial density distributions and $\langle R_{80} \rangle$ distributions are well described by the PYTHIA model (tune Perugia-2011). The fragmentation distributions are better described by HERWIG.

DOI: 10.1103/PhysRevD.91.112012 PACS numbers: 25.75.-q, 24.10.Nz, 25.75.Ag, 25.75.Dw

I. INTRODUCTION

Jets consist of collimated showers of particles resulting from the fragmentation of hard (high-momentum transfer Q) partons (quarks and gluons) produced in high-energy collisions. The production cross sections of jets were measured in detail in proton-antiproton ($p\bar{p}$) collisions at the Tevatron ($\sqrt{s} = 540$ GeV, 630 GeV, 1.8 TeV and 1.96 TeV) [1–11]. Measurements were also carried out recently at the CERN LHC at higher energies ($\sqrt{s} = 2.76$, 7 and 8 TeV) in proton-proton (pp) collisions [12–15]. Jet shape observables were previously measured by the CDF [16–18] and D0 [19] Collaborations in $p\bar{p}$ collisions and more recently by the ATLAS and CMS Collaborations in pp collisions [20–22]. The fragmentation functions of jets produced in $p\bar{p}$ collisions were reported by the CDF Collaboration [23]. Jet fragmentation in pp and Pb–Pb collisions at the LHC were reported by the ATLAS [12,24,25] and CMS [26] Collaborations. Jet production in e^+e^-, ep, $p\bar{p}$, and pp collisions is well described by perturbative Quantum Chromodynamics (pQCD) calculations. The measured jet properties are typically well reproduced by Monte Carlo (MC) generators such as PYTHIA [27], HERWIG [28,29], and PHOJET [30]. The unprecedented beam energy achieved at the Large Hadron Collider (LHC) in pp collisions enables an extension of jet production cross section and property measurements carried out at lower energies. Such measurements enable further tests of QCD and help in tuning of MC event generators.

In this paper, we present measurements of the jet production cross sections, jet fragmentation distributions, and transverse jet shape observables in pp collisions at $\sqrt{s} = 7$ TeV. The analysis is restricted to charged particle jets, i.e. jets reconstructed solely from charged particle momenta, hereafter called charged jets. ALICE has already reported measurements of charged jet production in Pb–Pb collisions at 2.76 TeV [31]. Charged jets are reconstructed with particles having p_T down to values as low as 0.15 GeV/c, thereby allowing us to test perturbative and nonperturbative aspects of jet production and fragmentation as implemented in MC generators. The measured particle spectra in jets reflect the jet fragmentation function, as summarized in [32] (Sec. 19). The jet shape distributions are related to the details of the parton shower process.

Jets also constitute an important probe for the study of the hot and dense QCD matter created in high-energy collisions of heavy nuclei. In such collisions, high p_T partons penetrate the colored medium and lose energy via induced gluon radiation and elastic scattering (see [33] and references therein). The measurements in pp collisions thus

[*]Full author list given at end of the article.

Published by the American Physical Society under the terms of the Creative Commons Attribution 3.0 License. Further distribution of this work must maintain attribution to the author(s) and the published article's title, journal citation, and DOI.

 © 2015 CERN, for the ALICE Collaboration

provide a baseline for similar measurements in nucleus–nucleus (A–A) and proton-nucleus (p–A) collisions.

Medium modifications of the parton shower may change the fragmentation pattern relative to the vacuum [34]. There are empirical indications [35] that the scale relevant to these effects is given by the medium temperature of the order of few hundred MeV rather than the hard scattering scale. At such small particle momenta, the jets measured experimentally in pp and A–A collisions also contain contributions from the underlying event (UE). In pp collisions [17], the UE includes gluon radiation in the initial state, the fragmentation of beam remnants and multiple parton interactions. In this study, we subtract the UE from the distributions measured in pp collisions, to allow for a meaningful comparison to models, because theoretical modeling of the underlying event is very complex. To disentangle UE and hard parton fragmentation into low momentum particles, we correct our measurements using a technique as described in Sec. VI D. This approach will also help to make eventually a comparison with data from A–A collisions, where the UE in addition includes hadrons from an expanding fireball.

This paper is organized as follows. Section II describes the experiment and detectors used for the measurements reported in this work. Details of the jet reconstruction algorithms and parameters are presented in Sec. III, while jet observables are defined and discussed in Sec. IV. Section V discusses the MC simulations carried out for comparisons of measured data to models, data corrections for instrumental effects, and systematic error studies. The procedures applied to correct for instrumental and UE effects are presented in Sec. VI. The methods used to evaluate systematic uncertainties of the measurements are discussed in Sec. VII. Results are presented and discussed in comparison with MC Event Generator simulations in Sec. VIII. Section IX summarizes the results and conclusions of this work.

II. EXPERIMENTAL SETUP AND DATA SAMPLE

The data used in this analysis were collected during the 2010 LHC run with the ALICE detector [36,37]. This analysis relies primarily on the Time Projection Chamber (TPC) [38], the Inner Tracking System (ITS) [39], and the V0 [40] subdetectors. The V0 and ITS are used for event selection. A minimum bias trigger is achieved by requiring at least one hit in either the V0 forward scintillators or in the two innermost Silicon Pixel Detector layers (SPD) of the ITS, in coincidence with an LHC bunch crossing. The efficiency for detecting inelastic events is about 85% [41]. The TPC and ITS are used for primary vertex and track reconstruction. Only events with a primary vertex within ± 10 cm along the beam direction from the nominal interaction point are analyzed to minimize dependencies of the TPC acceptance on the vertex position. The results reported in this paper are based on 177×10^6 minimum bias events corresponding to an integrated luminosity [41] of (2.9 ± 0.1) nb^{-1}.

The ALICE solenoidal magnet is operated with a magnetic field of 0.5 T that provides a good compromise between momentum resolution at high p_{T} and detection of low p_{T} particles. Charged tracks are reconstructed using the combined information from the TPC and the ITS utilizing a hybrid reconstruction technique described in [15] to assure uniform φ distribution. The acceptance for charged tracks is $|\eta| < 0.9$ over the full azimuth. This hybrid technique combines two distinct track classes: (i) tracks containing at least three hits (of up to six) in the ITS, including at least one hit in the SPD, and (ii) tracks containing fewer than three hits in the ITS, or no hit in the SPD. The momentum of tracks of class (i) is determined without a vertex constraint. The vertex constraint is however added for tracks of class (ii) to improve the determination of their transverse momentum. The track momentum resolution $\delta p_{\mathrm{T}}/p_{\mathrm{T}}$ is approximately 1% at $p_{\mathrm{T}} = 1$ GeV/c for all reconstructed tracks, and 4% at $p_{\mathrm{T}} = 40$ GeV/c for 95% of all tracks. For tracks without a hit in the ITS (5% of the track sample) the resolution is 7% at $p_{\mathrm{T}} = 40$ GeV/c. The analysis is restricted to tracks with a distance of closest approach (DCA) to the primary vertex smaller than 2.4 cm and 3.2 cm in the plane transverse to the beam and the beam direction, respectively, in order to suppress contributions from secondary particles produced by weak decays and interactions of primary particles with detector materials and beam pipe.

Tracks in the TPC are selected by requiring a p_{T} dependent minimum number of space points ranging from 70 (of up to 159) for $p_{\mathrm{T}} = 0.15$ GeV/c to 100 at $p_{\mathrm{T}} > 20$ GeV/c. A χ^2 cut on the track fit is applied. Secondary particles which are not produced at the primary vertex may acquire a wrong momentum when constrained to the vertex. Therefore, a χ^2 cut on the difference between the parameters of the track fit using all the space points in the ITS and TPC and using only the TPC space points with the primary vertex position as an additional constraint is applied. The track reconstruction efficiency for primary charged particles is approximately 60% at $p_{\mathrm{T}} = 0.15$ GeV/c and rises to a value of about 87% at 1 GeV/c and is approximately uniform up to 10 GeV/c beyond which it decreases slightly. The efficiency is uniform in azimuth and within the pseudorapidity range $|\eta| < 0.9$. Further details on the track selection procedure and tracking performance can be found in [15].

III. JET RECONSTRUCTION

The charged jet reconstruction is carried out using the infrared-safe and collinear-safe sequential recombination algorithms anti-k_{T} [42] and k_{T} [43,44] from the FastJet package [45] and a seedless infrared safe iterative cone based algorithm, named SISCone [46], to obtain the jet cross sections. The three jet finders are found to be in good

agreement within the uncertainties as discussed in Sec. VIII A. All other observables (as discussed in Sec. IV) are analyzed with anti-k_T only. Charged tracks with $p_T > 0.15$ GeV/c and within $|\eta| < 0.9$ are the inputs to the jet reconstruction algorithms. A boost invariant p_T recombination scheme is used to determine the transverse momenta of jets by adding the charged particle transverse momenta. Jets are reconstructed with resolution parameters $R = 0.2$, 0.3, 0.4, and 0.6 to enable a systematic study of the production cross section and shape properties, as well as to provide a suite of references for measurements performed in p–A and A–A collisions. The analyses reported in this work are restricted to jets detected within the range $|\eta| < (0.9 - R)$ in order to minimize edge effects in the reconstruction of jets and biases on jet transverse profile and fragmentation functions. The inclusive jet cross sections are reported as a function of p_T in the interval $20 < p_T^{\mathrm{jet,ch}} < 100$ GeV/c. The properties of the charged jet with the highest p_T in the event, the so called *leading jet*, are presented in the same p_T interval.

IV. JET OBSERVABLES

The results are reported for a suite of charged jet properties including inclusive differential jet cross section, charged particle multiplicity in leading jets ($\langle N_{\mathrm{ch}} \rangle$), leading jet size ($\langle R_{80} \rangle$), radial distribution of p_T within the leading jet ($\langle \mathrm{d}p_T^{\mathrm{sum}}/\mathrm{d}r \rangle$), and jet fragmentation distributions (F^{p_T}, F^z, F^ξ). The definition of these observables and the methods used to measure them are presented in this section. Correction techniques applied to measured raw distributions to account for instrumental effects (including the detector acceptance and resolution), as well as the UE, are discussed in Sec. VI. All observables reported in this work are corrected to particle level as defined in Sec. V.

The differential jet cross section is evaluated using the following relation:

$$\frac{\mathrm{d}^2\sigma^{\mathrm{jet,ch}}}{\mathrm{d}p_T \mathrm{d}\eta}(p_T^{\mathrm{jet,ch}}) = \frac{1}{\mathcal{L}^{\mathrm{int}}} \frac{\Delta N_{\mathrm{jets}}}{\Delta p_T \Delta \eta}(p_T^{\mathrm{jet,ch}}), \quad (1)$$

where $\mathcal{L}^{\mathrm{int}}$ is the integrated luminosity and ΔN_{jets} the number of jets in the selected intervals of Δp_T and $\Delta\eta$.

The charged particle multiplicity in leading jets, N_{ch}, is defined as the number of charged particles found within the leading jet cone. Results for the mean charged particle multiplicity, $\langle N_{\mathrm{ch}} \rangle$, computed in bins of jet p_T are presented for resolution parameter values $R = 0.2$, 0.4, and 0.6.

The size of the leading jet, R_{80}, is defined as the radius in the $\Delta\eta - \Delta\varphi$ space that contains 80% of the total p_T found in the jet cone. Results for the mean value, $\langle R_{80} \rangle$, are presented as a function of jet p_T for resolution parameter values $R = 0.2$, 0.4, and 0.6.

The distribution of p_T density, $\mathrm{d}p_T^{\mathrm{sum}}/\mathrm{d}r$, within a leading jet is measured as a function of the distance $r = \sqrt{(\Delta\eta)^2 + (\Delta\varphi)^2}$ from the jet direction. The momentum density is calculated jet by jet as a scalar sum of the transverse momenta, p_T^{sum}, of all charged particles produced in annular regions of width Δr at radius r centered on the jet direction. The mean value of the momentum density, $\langle \mathrm{d}p_T^{\mathrm{sum}}/\mathrm{d}r \rangle$, is evaluated as a function of r using the following relation:

$$\left\langle \frac{\mathrm{d}p_T^{\mathrm{sum}}}{\mathrm{d}r} \right\rangle (r) = \frac{1}{\Delta r} \frac{1}{N_{\mathrm{jets}}} \sum_{\mathrm{i}=1}^{N_{\mathrm{jets}}} p_T^{\mathrm{i}}(r - \Delta r/2, r + \Delta r/2) \quad (2)$$

where $p_T^{\mathrm{i}}(r - \Delta r/2, r + \Delta r/2)$ denotes the summed p_T of all tracks of jet i, inside the annular ring between $r - \Delta r/2$ and $r + \Delta r/2$. The mean value is reported in bins of jet p_T for resolution parameter values $R = 0.2, 0.4$, and 0.6. N_{jets} denotes the number of jets per bin.

The fragmentation of the leading jet is reported based on the distributions

$$F^{p_T}(p_T, p_T^{\mathrm{jet,ch}}) = \frac{1}{N_{\mathrm{jets}}} \frac{\mathrm{d}N}{\mathrm{d}p_T}, \quad (3)$$

$$F^{z}(z^{\mathrm{ch}}, p_T^{\mathrm{jet,ch}}) = \frac{1}{N_{\mathrm{jets}}} \frac{\mathrm{d}N}{\mathrm{d}z^{\mathrm{ch}}}, \quad (4)$$

$$F^{\xi}(\xi^{\mathrm{ch}}, p_T^{\mathrm{jet,ch}}) = \frac{1}{N_{\mathrm{jets}}} \frac{\mathrm{d}N}{\mathrm{d}\xi^{\mathrm{ch}}}, \quad (5)$$

where N is the number of charged particles. The scaled p_T variables $z^{\mathrm{ch}} = p_T^{\mathrm{particle}}/p_T^{\mathrm{jet,ch}}$ and $\xi^{\mathrm{ch}} = \log(1/z^{\mathrm{ch}})$ are calculated jet by jet for each track. In contrast to the definition in [32], the energy carried by neutral particles is not contained in the jet momentum. The (scaled) p_T spectra of the jet constituents are normalized per jet and presented in bins of jet p_T. F^{p_T}, F^z and F^ξ are complementary representations: the particle p_T spectra F^{p_T} are less sensitive to uncertainties in the jet energy scale and may be more suitable as a reference for future measurements in nuclear collisions than the standard representation F^z, whereas the F^ξ distributions emphasize fragmentation into low momentum constituents and are particularly suited to demonstrate QCD coherence effects [47,48].

In this work, the averages $\langle N_{\mathrm{ch}} \rangle$, $\langle R_{80} \rangle$, and $\langle \mathrm{d}p_T^{\mathrm{sum}}/\mathrm{d}r \rangle$ are referred to as jet shape observables (jet shapes) and F^{p_T}, F^z and F^ξ as fragmentation distributions.

V. MONTE CARLO SIMULATIONS

Instrumental effects, such as the limited particle detection efficiency and the finite track momentum resolution, induce momentum dependent particle losses and impact the jet energy scale and structures of the observables reported in this work. The effect of the detector response is studied using the simulation of the ALICE detector performance for particle detection and jet reconstruction. Simulated

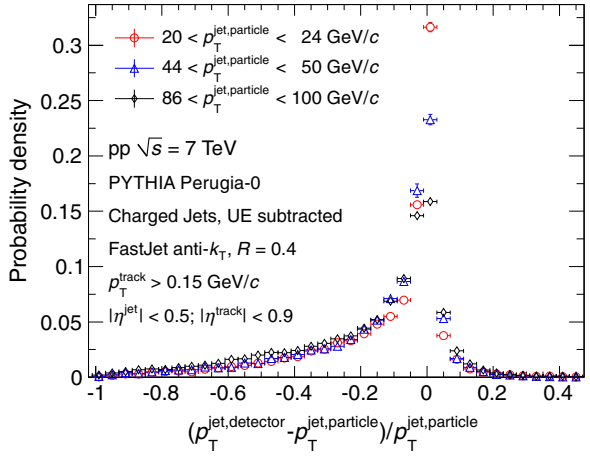

FIG. 1 (color online). Probability distribution of the relative momentum difference of simulated ALICE detector response to charged jets in pp collisions at $\sqrt{s} = 7$ TeV for three different $p_T^{jet,particle}$ intervals. Charged jets are simulated using PYTHIA Perugia-0 and reconstructed with the anti-k_T jet finding algorithm with $R = 0.4$.

events are generated with PYTHIA 6.425 [27] (tune Perugia-0 [49]) and the produced particles are transported with GEANT3 [50]. The simulated and real data are analyzed with the same reconstruction algorithms and using the same kinematic cuts ($p_T > 0.15$ GeV/c, $|\eta| < 0.9$) on produced particles. Jets reconstructed based directly on momenta of charged particles ($p_T > 0.15$ GeV/c, $|\eta| < 0.9$) produced by MC generators are hereafter referred to as *particle level* jets whereas those obtained after processing the generator outputs through GEANT and the ALICE reconstruction software are referred to as *detector level* jets. As the data are corrected for instrumental effects, their comparison with simulation is done at particle level only.

The detector response to simulated charged jets with $R = 0.4$ is illustrated in Fig. 1, showing on a jet-by-jet basis the probability distribution of the relative difference between the charged jet p_T at the particle level ($p_T^{jet,particle}$) and at the detector level ($p_T^{jet,detector}$). The probability distribution is shown for three different $p_T^{jet,particle}$ intervals. The distributions have a pronounced maximum at zero ($p_T^{jet,detector} = p_T^{jet,particle}$). The tracking p_T resolution induces upward and downward fluctuations with equal probability, whereas the finite detection efficiency of charged particles results in an asymmetric response. As a function of $p_T^{jet,particle}$, the probability that $p_T^{jet,detector}$ is smaller than $p_T^{jet,particle}$ varies between 88% and 92% and the mean value of the distribution varies between -14% and -24%.

The event generators PHOJET 1.12.1.35 [30], HERWIG 6.510 [28,29], and several PYTHIA tunes are used for comparisons to data and for systematic investigations of the sensitivity of the MC correction factors to variations of the detector response as well as to jet fragmentation and hadronization patterns. PYTHIA, PHOJET, and HERWIG utilize different approaches to describe the parton shower and hadronization process. HERWIG makes of angular ordering a direct part of the evolution process and thereby takes correctly into account coherence effects in the emission of soft gluons. PYTHIA 6.4 is instead based on transverse-momentum-ordered showers [51] in which angular ordering is imposed by an additional veto. PHOJET generates angular ordered initial-state radiation, whereas for final state radiation the mass-ordered PYTHIA shower algorithm is used. Hadronization in PYTHIA and PHOJET proceeds via string breaking as described by the Lund model [52], whereas HERWIG uses cluster fragmentation. The PYTHIA Perugia tune variations, beginning with the central tune Perugia-0 [49], are based on LEP, Tevatron, and SPS data. The Perugia-2011 family of tunes [49] and the ATLAS Minimum Bias tune AMBT1 [53] belong to the first generation of tunes that also use LHC pp data at $\sqrt{s} = 0.9$ and 7 TeV with slight variations of the parameters controlling the modeling of the UE and fragmentation. Compared to the central Perugia-2011 tune, AMBT1 uses a lower value of the infrared regularization scale for multiple partonic interactions resulting in higher UE activity. It also uses a probability density of sum of two Gaussians for the matter distribution inside the proton and a higher nonperturbative color-reconnection strength for string fragmentation. The HERWIG generator version and PYTHIA tunes used in this work utilize the CTEQ5L parton distributions [54], except for PYTHIA tune AMBT1 which uses MRST 2007LO* [55]. PHOJET uses GRV94 [56].

VI. CORRECTIONS

Two classes of correction techniques are used to account for instrumental effects in the measurements reported in this work. The techniques are known as bin-by-bin correction and Bayesian unfolding [57]. A third technique based on singular value decomposition (SVD) [58] is also used as a cross check. The techniques and their comparative merits are presented in the following subsections. Corrections for contamination from secondary particles and UE are discussed in Secs. VI C and VI D, respectively.

The jet shapes and fragmentation distributions are corrected using the bin-by-bin method, while the cross sections are corrected with the Bayesian unfolding technique. All observables are corrected for secondaries contamination. All observables, except $\langle R_{80} \rangle$, are also corrected for UE contamination.

A. Bin-by-bin correction method

The bin-by-bin correction method is used to correct the jet shape observables and fragmentation functions. To validate the method, it is also applied to the jet cross sections. It utilizes MC simulations as described in Sec. V

and is based on ratios of values for observables obtained at particle (generator) level and detector level as a function of variable $\mathbf{x}$. In this work, $\mathbf{x}$ can be one-dimensional (e.g. jet p_{T} in case of the jet spectra) or two-dimensional (e.g. jet p_{T} and particle p_{T} in case of the fragmentation distributions). Let $O_{\mathrm{mc}}^{\mathrm{part}}(\mathbf{x})$ be the observable value at the particle level, and $O_{\mathrm{mc}}^{\mathrm{det}}(\mathbf{x})$ the value obtained at the detector level. The correction factors are defined as the ratio of the particle and detector level values of $O_{\mathrm{mc}}^{\mathrm{part}}(\mathbf{x})$ and $O_{\mathrm{mc}}^{\mathrm{det}}(\mathbf{x})$ in bins of $\mathbf{x}$. The corrected measurements, $O_{\mathrm{data}}^{\mathrm{corrected}}$, are obtained bin-by-bin by multiplying the raw (uncorrected) values, $O_{\mathrm{data}}^{\mathrm{uncorrected}}$, as follows,

$$O_{\mathrm{data}}^{\mathrm{corrected}}(\mathbf{x}) = O_{\mathrm{data}}^{\mathrm{uncorrected}}(\mathbf{x}) \frac{O_{\mathrm{mc}}^{\mathrm{part}}(\mathbf{x})}{O_{\mathrm{mc}}^{\mathrm{det}}(\mathbf{x})}. \quad (6)$$

The correction factors depend on the shape of the simulated jet spectrum and fragmentation distributions. Systematic uncertainties related to the accuracy with which data are reproduced by the simulations are discussed in Sec. VII B.

Correction factors obtained for the jet p_{T} spectra range from 25% to 50% and reach a maximum at 100 GeV/c. The bin-by-bin corrections applied to jet shape observables include subtraction of contamination associated with the production of secondary particles within the detector. Correction factors obtained for $\langle N_{\mathrm{ch}} \rangle$ at $R = 0.2$ (0.4, 0.6) are of the order of 2%–6% (3%–5%, 4%–6%) while for $\langle R_{80} \rangle$ at $R = 0.2\,(0.4, 0.6)$ they are found in the range 5%–7% (2%–10%, 4%–9%). Correction factors applied on radial momentum densities have a maximum value of 12%(15%, 19%) at $R = 0.2$ (0.4, 0.6). In contrast, for the fragmentation distributions, the bin-by-bin correction and the correction for the contamination from secondaries, discussed in Sec. VI C, are carried out in separate steps. The typical value of the corrections at the maximum of the F^{ξ} distribution is of the order of few percent only. The correction factors for $F^{p_{\mathrm{T}}}$ and F^{z} are largest at low particle p_{T} (up to 50%), where the tracking efficiency is smallest, and at the highest z^{ch} (up to 40%) where the impact of the track momentum resolution is strong and detector effects at the track level strongly influence the reconstructed jet momentum.

B. Unfolding using response matrix inversion techniques

Instrumental effects associated with acceptance, particle losses due to limited efficiency, and finite momentum resolution are modeled using a detection response matrix, which is used to correct observables for these effects. The jet p_{T} response matrix is determined by processing MC events through a full ALICE detector simulation as described in Sec. V. The particle level (true), $T(t)$, and detector level (measured), $M(m)$, p_{T} spectra of the leading jet are both subdivided in 11 bins in the interval $20 < p_{\mathrm{T}}^{\mathrm{jet,ch}} < 100$ GeV/c. The matrix elements R_{mt} express the conditional probability of measuring a jet p_{T} in bin, m given a true value in bin, t. The measured distribution, M, can thus be estimated by multiplying the true distribution, T, by the response matrix,

$$M = RT. \quad (7)$$

Experimentally, the unfolding problem involves the determination of T given M. This is symbolically written as

$$T = R^{-1}M. \quad (8)$$

However the matrix R may be singular and can not always be inverted analytically. Consequently, other numerical techniques are needed to obtain the true, physically meaningful, distribution T given a measured distribution M. Furthermore, the exact solution, even if it exists, is usually unstable against small variations in the initial estimates of the measured distribution, and oscillating due to finite statistics in the measured distribution. This problem can be overcome using a regularization condition based on *a priori* information about the solution.

The Bayesian unfolding technique [57] is an iterative method based on Bayes' theorem. Given an initial hypothesis (*a prior*), P_t, with $t = 1, \ldots, n$, for the true momentum and reconstruction efficiency, ε_t, Bayes' theorem provides an estimator of the inverse response matrix elements, $\tilde{R}_{tm}$,

$$\tilde{R}_{tm} = \frac{R_{mt}P_t}{\varepsilon_t \sum_{t'} R_{mt'} P_{t'}}. \quad (9)$$

The measured distribution, M_m, is thus unfolded as follows

$$P'_t = \sum_m \tilde{R}_{tm} M_m, \quad (10)$$

to obtain *a posterior* estimator, P'_t, of the true distribution. The inversion is improved iteratively by recursively using posterior estimators to update and recalculate the inversion matrix. The number of iterations serves as a regularization parameter in the unfolding procedure. For jet spectra studies, the measured spectra are used as prior and convergence is obtained typically after three iterations.

As an additional cross check, the analysis of charged jet cross sections is also carried out with the RooUnfold implementation of the SVD unfolding technique [58,59] using raw measured spectra as prior distributions. The performance of the Bayesian unfolding, SVD unfolding, and bin-by-bin correction methods are compared based on PYTHIA Perugia-0 simulated jets. The three methods produce results that are found to be within 4% of the truth distribution. The cross sections reported in this work are obtained with the Bayesian unfolding method.

C. Contamination from secondary particles

Charged secondary particles are predominantly produced by weak decays of strange particles (e.g. K^0_{S} and Λ), decays of charged pions, conversions of photons from neutral pion decays and hadronic interactions in the detector material. The

charged jet transverse momentum, jet shapes and fragmentation distributions include by definition only primary charged particles (prompt particles produced in the collisions and all decay products, except products from weak decays of strange particles such as K^0_S and Λ). Secondary particles introduce ambiguities in the jet energy scale and contribute to the raw reconstructed multiplicity, momentum density, and fragmentation distributions. Although their contribution is minimized by the analysis cuts described in Sec. II, the measured distributions nonetheless must be corrected for a small residual contamination. The subtraction of the secondary particle contamination is implicitly included in the bin-by-bin correction applied for measurements of jet shape observables. It is however carried out separately and explicitly in the measurements of the fragmentation function. The contribution of secondaries is estimated from MC simulations, separately for each bin in jet p_T and particle p_T, z^{ch} and ξ^{ch}. The correction applied to the measured fragmentation functions is highest, up to 35%, at small p_T and large ξ^{ch}. It amounts to few percent only when averaged over all jet constituents. To enhance the low strangeness yield in the PYTHIA Perugia-0 simulations to the level observed in data, the contamination estimate is multiplied by a data-driven correction factor based on measurements [60] of strange particle production in non-single-diffractive events by the CMS Collaboration and simulations from [61]. The contamination of secondaries from strange particle decays is small, and the effect of the strangeness scaling on the final result is less than 1%. No scaling is applied on the correction to the jet spectrum and jet shape observables.

D. Underlying event subtraction

There is no strict definition of the Underlying Event. Operationally, it corresponds to all particles produced in an event that are not an integral part of a jet or produced directly by hard scattering of partons. The ATLAS [62,63], CMS [64] and ALICE [65] Collaborations have already published studies of UE in pp collisions at $\sqrt{s} = 7$ TeV. In this work, a similar method is adopted to determine the UE yield and correct the measured jet observables for this source of contamination.

The UE particle yield is estimated event-by-event based on circular regions perpendicular to the measured jet cones. The circular regions have the same size as the jet resolution parameter and are placed at the same pseudorapidity as the leading jet but offset at an azimuthal angle $\Delta\varphi = \pi/2$ relative to the jet axis.

For the jet cross section measurements, the UE is subtracted on a jet-by-jet basis prior to unfolding and the same treatment is applied to jets obtained from simulations before jet response matrix is created.

In the case of the fragmentation and jet shape observables, no correction for the UE contribution to the reconstructed jet energy is applied, but the UE contribution to the measured distributions in each bin of jet p_T is subtracted. The p_T spectra of particles in the perpendicular cone are accumulated and averaged over many events. To account for variations of the cone size of the anti-k_T jets, the spectra are weighted jet by jet with the ratio of the cone size, determined by FastJet, to the nominal aperture of πR^2 for a jet with resolution parameter R. The difference between the weighted and unweighted UE distributions is at the level of 1%. The ξ^{ch} variable is computed jet-by-jet for each particle using the transverse momentum of the leading jet. The radial p_T sum distributions are obtained relative to the axis of the perpendicular cone.

The algorithms used for jet reconstruction are sensitive to statistical fluctuations of the particle density which are possibly enhanced by local variations of the detection efficiency and secondary particle production. This reconstruction bias may differ for the jet region and the UE region. Hence, the UE distributions are corrected first for tracking efficiency, resolution and contamination from secondary particles. The fully corrected distributions are then subtracted in bins of the leading jet transverse momentum. The correction is smaller than 2.5% of the charged jet energy, but it is considerable for the fragmentation distributions at the lowest track momentum and highest ξ^{ch}, where the ratio of UE background to fragmentation signal takes values up to 2.5. No self-consistent technique exists to subtract the UE in the $\langle R_{80}\rangle$ measurements, these measurements are therefore reported without correction for UE contamination. However, comparing the radial $\langle dp_T^{sum}/dr\rangle$ distributions before and after UE subtraction, the increase in jet size $\langle R_{80}\rangle$ due to the UE is estimated to be of the order of few percent only. The systematic uncertainties for not performing the UE subtraction are thus found negligible compared to other sources of errors in the measurements of $\langle R_{80}\rangle$.

VII. ESTIMATION OF SYSTEMATIC UNCERTAINTIES

A summary of all systematic uncertainties for selected bins is given in Table I for the cross section measurements, and in Table II for the $\langle N_{ch}\rangle$, $\langle R_{80}\rangle$, $\langle dp_T^{sum}/dr\rangle$, F^{p_T}, F^{p_T} and F^z distributions. The uncertainties given in each column of the table are described in this section.

A. Tracking efficiency and resolution

Uncertainties associated with the momentum resolution and charged track reconstruction efficiency lead to systematic uncertainties in measurements of the jet cross section, jet shapes, and jet fragmentation functions.

The relative systematic uncertainty on tracking efficiency is estimated to be 5% based on several variations of cuts used in the track selection introduced earlier. The relative systematic uncertainty on the track momentum resolution amounts to 20% [66].

TABLE I. Summary of systematic uncertainties for selected bins in selected cross section distributions.

Distribution	Bin (GeV/c)	Track efficiency (%)	Track p_{T} resolution (%)	Unfolding (%)	Normalization (%)	Secondaries (%)	Total (%)
$\frac{\mathrm{d}^2\sigma^{\mathrm{jet,ch}}}{\mathrm{d}p_{\mathrm{T}}\mathrm{d}\eta}$ $(R = 0.2)$	20–24	$^{+4.6}_{-4.2}$	4.0	3.0	3.5	1.9	$^{+7.8}_{-7.6}$
	50–58	$^{+22.1}_{-10.5}$	4.0	1.6	3.5	2.5	$^{+23.0}_{-12.2}$
	86–100	$^{+26.0}_{-15.3}$	4.0	5.2	3.5	2.8	$^{+27.1}_{-17.2}$
$\frac{\mathrm{d}^2\sigma^{\mathrm{jet,ch}}}{\mathrm{d}p_{\mathrm{T}}\mathrm{d}\eta}$ $(R = 0.4)$	20–24	$^{+7.5}_{-4.5}$	4.0	3.0	3.5	2.1	$^{+9.9}_{-7.9}$
	50–58	$^{+23.2}_{-10.6}$	4.0	1.4	3.5	2.5	$^{+24.0}_{-12.2}$
	86–100	$^{+24.9}_{-15.0}$	4.0	5.6	3.5	2.7	$^{+26.2}_{-17.2}$
$\frac{\mathrm{d}^2\sigma^{\mathrm{jet,ch}}}{\mathrm{d}p_{\mathrm{T}}\mathrm{d}\eta}$ $(R = 0.6)$	20–24	$^{+11.1}_{-5.3}$	4.0	6.6	3.5	2.3	$^{+14.2}_{-10.3}$
	50–58	$^{+22.6}_{-14.3}$	4.0	1.9	3.5	2.6	$^{+23.4}_{-15.6}$
	86–100	$^{+23.7}_{-13.7}$	4.0	6.0	3.5	2.7	$^{+25.1}_{-16.1}$

TABLE II. Summary of systematic uncertainties for selected bins in selected jet shape and fragmentation distributions for $R = 0.4$.

Distribution	Bin	Track efficiency (%)	Track p_{T} resolution (%)	Bin-by-bin correction (%)	UE (%)	Secondaries (%)	Total (%)
$\langle N_{\mathrm{ch}} \rangle$	20–25 GeV/c	$^{+5.8}_{-5.0}$	$^{+4.0}_{-3.5}$	$^{+0.7}_{-0.9}$	0.8	Negligible	$^{+7.1}_{-6.2}$
	80–100 GeV/c	$^{+5.8}_{-5.0}$	$^{+4.0}_{-3.5}$	$^{+0.7}_{-0.9}$	0.5	Negligible	$^{+7.1}_{-6.2}$
$\langle R_{80} \rangle$	20–25 GeV/c	$^{+6.1}_{-5.5}$	$^{+3.6}_{-4.3}$	$^{+1.7}_{-1.7}$	—	—	$^{+7.2}_{-7.2}$
	80–100 GeV/c	$^{+6.1}_{-5.5}$	$^{+3.6}_{-4.3}$	$^{+1.7}_{-1.7}$	—	—	$^{+7.2}_{-7.2}$
$\langle \frac{\mathrm{d}p_{\mathrm{T}}^{\mathrm{sum}}}{\mathrm{d}r} \rangle$ $20 < p_T^{\mathrm{jet,ch}} < 30$ GeV/c	0.00–0.04	$^{+8.1}_{-6.5}$	$^{+5.9}_{-2.4}$	$^{+2.9}_{-3.1}$	Negligible	Negligible	$^{+10.4}_{-7.5}$
	0.20–0.24	$^{+8.1}_{-6.5}$	$^{+5.9}_{-2.4}$	$^{+2.9}_{-3.1}$	0.3	Negligible	$^{+10.5}_{-7.6}$
	0.36–0.40	$^{+8.1}_{-12.0}$	$^{+5.9}_{-2.4}$	$^{+2.9}_{-3.1}$	15.0	Negligible	$^{+18.3}_{-19.6}$
$\langle \frac{\mathrm{d}p_{\mathrm{T}}^{\mathrm{sum}}}{\mathrm{d}r} \rangle$ $60 < p_T^{\mathrm{jet,ch}} < 80$ GeV/c	0.00–0.04	$^{+10.6}_{-5.1}$	$^{+5.6}_{-6.5}$	$^{+3.7}_{-3.4}$	Negligible	Negligible	$^{+12.6}_{-8.9}$
	0.20–0.24	$^{+10.6}_{-5.1}$	$^{+5.6}_{-6.5}$	$^{+3.7}_{-3.4}$	0.4	Negligible	$^{+12.6}_{-9.0}$
	0.36–0.40	$^{+10.6}_{-5.1}$	$^{+5.6}_{-6.5}$	$^{+3.7}_{-3.4}$	1.6	Negligible	$^{+12.7}_{-9.1}$
$F^{p_{\mathrm{T}}}$ $20 < p_T^{\mathrm{jet,ch}} < 30$ GeV/c	0–1 GeV/c	5.0	0.1	0.7	3.3	3.2	6.8
	6–7 GeV/c	0.8	Negligible	2.3	Negligible	0.5	2.4
	18–20 GeV/c	9.9	0.5	6.0	Negligible	0.4	11.6
$F^{p_{\mathrm{T}}}$ $60 < p_T^{\mathrm{jet,ch}} < 80$ GeV/c	0–5 GeV/c	5.2	0.3	0.2	0.8	2.1	5.7
	20–30 GeV/c	1.4	Negligible	3.7	Negligible	0.6	4.0
	50–60 GeV/c	10.5	3.5	9.6	Negligible	0.6	14.6
F^{z} $20 < p_T^{\mathrm{jet,ch}} < 30$ GeV/c	0–0.1	4.7	1.6	0.2	1.6	1.4	5.2
	0.3–0.4	0.4	Negligible	2.7	Negligible	0.3	2.8
	0.9–1.0	15.5	1.1	4.8	Negligible	0.6	16.3
F^{z} $60 < p_T^{\mathrm{jet,ch}} < 80$ GeV/c	0–0.1	5.0	0.3	0.3	0.7	1.3	5.3
	0.3–0.4	1.2	0.2	3.7	Negligible	0.4	3.9
	0.8–1.0	13.8	3.1	6.1	Negligible	1.2	15.4
F^{ξ} $20 < p_T^{\mathrm{jet,ch}} < 30$ GeV/c	0–0.4	9.9	0.5	4.6	Negligible	0.7	10.9
	0.8–1.2	0.6	Negligible	3.0	Negligible	0.5	3.1
	4.8–5.3	5.1	0.7	0.9	15.3	7.8	17.9
F^{ξ} $60 < p_T^{\mathrm{jet,ch}} < 80$ GeV/c	0–1.0	5.0	0.5	3.9	Negligible	0.7	6.4
	1.0–2.0	1.3	0.4	3.4	Negligible	0.6	3.8
	5.0–6.2	5.7	0.2	0.7	6.5	6.2	10.6

In order to evaluate the effect of these uncertainties on the measured jet cross sections, the corresponding rescaled response matrix is used to unfold the spectra. For the jet shape and fragmentation observables, the impact of the finite detector efficiency and momentum resolution on the bin-by-bin correction factors is estimated by applying parametrized detector response to PYTHIA events clustered with FastJet, and varying the efficiency and resolution independently. Systematic uncertainties for the jet particle multiplicity and jet shape observables are given in Table II for a resolution parameter $R = 0.4$. For larger (smaller) R, a moderate increase (decrease) of the uncertainties is observed related to tracking efficiency. For the fragmentation distributions, variations of the momentum resolution induce the most significant changes at high track p_{T}. The systematic uncertainties due to the efficiency variations are largest at the highest z^{ch} and smallest at intermediate values.

B. Bin-by-bin correction

The data correction methods used in this work are largely based on tune Perugia-0 of the PYTHIA event generator. The particular structure of jets produced by PYTHIA might however conceivably affect the magnitude, and dependencies of the correction factors on the jet momentum, particle momentum, or radial dependence r. The possible impact of such event generator dependencies is examined by comparing the amplitude of the bin-by-bin corrections obtained with PYTHIA tunes Perugia-0 and Perugia-2011, with those obtained with the HERWIG generator. This is accomplished with a parametrized detector response and the anti-k_{T} jet finder. In addition, the impact of modifications of the jet fragmentation is studied by artificially duplicating and removing jet particles with a momentum dependent probability. The variations are constrained to be at a similar level as the differences observed between simulations and data reaching up to a factor of 2.5 for values of z^{ch} close to 1 in the fragmentation distributions. The charged particle multiplicity is affected by ~30%. The resulting systematic uncertainties are largest for high values of z^{ch} and track p_{T} and small values of ξ^{ch}.

As an independent check, a closure test with a two-dimensional folding technique is carried out on the fragmentation distributions from an inclusive jet sample (comprising leading and subleading jets). A response matrix in bins of generated and reconstructed jet p_{T} and particle (scaled) transverse momentum is used to fold the corrected results back to the uncorrected level. Since the folding method has negligible dependence on the event generator, the comparison of the folded to the original distributions reveals possible biases of the bin-by-bin correction. The observed nonclosure at the level of few percent is consistent with the systematic uncertainty assigned to the bin-by-bin correction from modifications of the fragmentation pattern.

C. Response unfolding

The unfolding techniques used in this work correct the measured jet spectra for the detector response. The limited measurement resolution, discussed in Sec. V, results in a small, but finite, probability for bin migration of the reconstructed jet momentum relative to the true value. Consequently, the unfolding introduces a correlation between neighboring bins of the corrected spectrum, and statistical fluctuations in the measured data result in a spectral shape systematic uncertainty. To assess this uncertainty, the raw jet spectra are smeared by a Gaussian function with a width given by the statistical uncertainty in the given momentum bin. The resulting spectra are then unfolded and the systematic uncertainty is evaluated as a spread of the corrected spectra. The value of this systematic uncertainty increases roughly linearly with $p_{\mathrm{T}}^{\mathrm{jet,ch}}$, reaching a maximum value of ~7% at $p_{\mathrm{T}}^{\mathrm{jet,ch}} \approx 100$ GeV/c.

D. Underlying event subtraction

In this work, we use perpendicular cones to measure and subtract the UE as described in Sec. VI D. However, there is no unique prescription on how to determine the UE. In a prior, trigger hadron based, UE analysis by the ALICE Collaboration [65], a geometrically different definition of the transverse region was used. The charged particle transverse momentum densities obtained in our analysis are consistent with the saturation values in the transverse region measured in [65]. In [67], the UE was estimated from dijet events and imposing an additional veto on a third jet. An alternative simulation to estimate and subtract the UE in a similar way is performed using particle level output from a MC event generator. The UE is measured from events with a dijet in the detector acceptance, to understand if and how the nonleading jet affects the UE estimate, rejecting events with additional charged jets with a p_{T} exceeding 12 GeV/c. The resulting difference on the fragmentation distributions is used to assign a 5% systematic uncertainty to the estimated UE. The resulting systematic uncertainty on the fragmentation distributions is highest at low transverse momenta. Systematic uncertainties on $\langle \mathrm{d}p_{\mathrm{T}}^{\mathrm{sum}}/\mathrm{d}r \rangle$ are largest at large distances r in the jet p_{T} interval 20–30 GeV/c. The uncertainty increases for higher values of the resolution parameter R. Systematic uncertainties on the measured charged jet cross sections are smaller than 1% and considered negligible.

The anti-k_{T} jet finder typically produces circular jet cones, and the UE contribution to the jet shapes and fragmentation distributions is evaluated consistently in circular cones. In individual jets, particles may however be added at a distance $r \geq R$ thereby giving rise to a convex deformation of the cone. Concave deformations might also occur. The dependence of the fragmentation distributions on the cone shape is checked by repeating the analysis using only tracks in an ideal cone around the jet axis. In this

case no jet area scaling of the UE is applied. The low-momentum particle yield is most affected: at high jet radii, low z^{ch} fragmentation dominates over high z^{ch} fragmentation. In addition, the probability to collect a soft particle from the UE is comparatively higher than at small r. The observed effect is negligibly small: a maximum depletion of 4% of the particle yield at the highest ξ^{ch} in the smallest jet momentum bin is observed. Considerably smaller variations are found for all other jet momenta and ξ^{ch} bins. The effect is reproduced in MC simulations, and no systematic uncertainty is associated to the jet cone shape.

E. Cross section normalization

The determination of luminosity and related systematic uncertainties are discussed in [68,69]. A normalization uncertainty of 3.5% is assigned to the cross section measurement.

F. Contamination from secondary particles

The reconstructed primary particles originate from the main interaction vertex and have a nonzero distance of closest approach DCA because of finite resolution effects. The DCA of secondaries however spans a much broader range of values. Reducing the maximum allowed DCA value reduces contaminations from secondaries but also reduces the detection efficiency of primary particles. In this analysis, primary particles are selected requiring a small DCA as discussed in Sec. II, and a correction for the residual contribution of secondary particles is applied, as explained in Sec. VI C. The systematic uncertainty associated to the correction is estimated by reducing the maximum allowed DCA used in the selection of primary tracks by more than a factor of 9 using a p_{T} dependent cut. The resulting fragmentation distributions are corrected consistently for contamination and cut efficiency and residual differences in the fully corrected spectra are assigned as systematic uncertainty. The highest uncertainty is found for large values of ξ^{ch}.

The dependence of the correction on the strange particle yield in the PYTHIA Perugia-0 simulations is estimated from comparison to data as explained in Sec. VI C. The effect on the jet cross sections is less than 3% and is assigned as systematic uncertainty. For the jet shape observables it is negligible.

VIII. RESULTS

A. Comparison of jet finding algorithms

Figure 2 (top panel) shows the differential cross sections of charged jet production measured in pp collisions at $\sqrt{s} = 7$ TeV using the k_{T}, anti-k_{T}, and SISCone jet finding algorithms. The distributions are obtained with a resolution parameter, $R = 0.4$, for jets in the pseudorapidity range $|\eta^{\mathrm{jet}}| < 0.5$, and transverse momenta from 20 to 100 GeV/c. The bottom panel of the figure displays the ratios between the cross sections obtained with the k_{T}, and

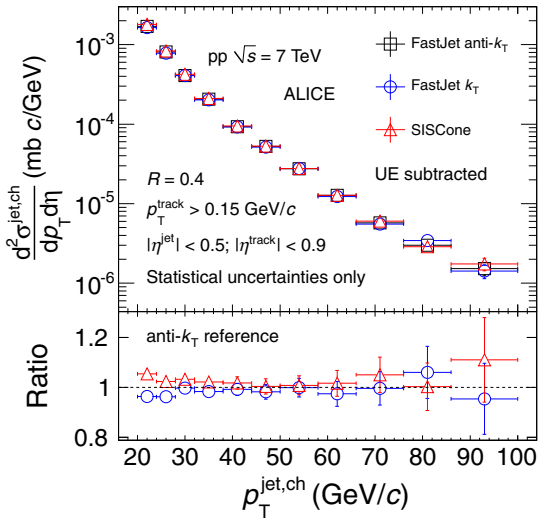

FIG. 2 (color online). Top panel: Charged jet cross sections in pp collisions at $\sqrt{s} = 7$ TeV. Symbols correspond to different algorithms used for jet reconstruction. Bottom panel: Ratios between jet cross sections obtained by k_{T}, and SISCone to that obtained by anti-k_{T}.

SISCone algorithms to those obtained with the anti-k_{T} as a function of the jet transverse momentum. For a correct treatment of statistical correlations between the numerator and denominator, the data were divided into fully correlated and uncorrelated subsets. The distributions are corrected using the bin-by-bin correction procedure described in Sec. VI A. The ratios of the jet cross sections are consistent with unity over nearly the entire range of jet transverse momenta spanned by this analysis. A significant deviation of 5% is observed only in the lowest p_{T} bin ($p_{\mathrm{T}}^{\mathrm{jet,ch}} = 20$–$24$ GeV/c) between the SISCone and anti-k_{T}

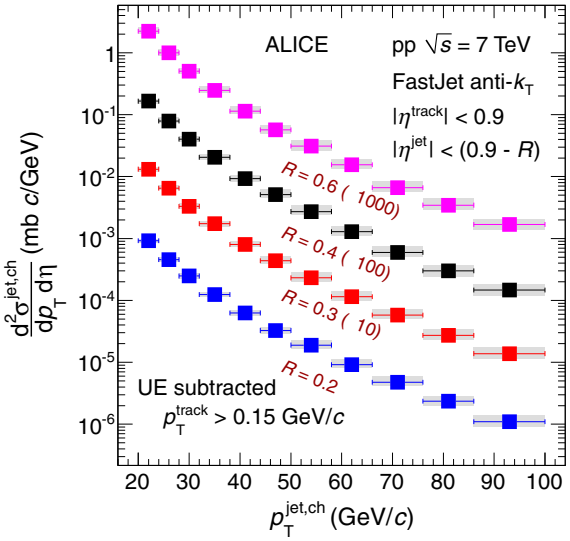

FIG. 3 (color online). Inclusive charged jet cross sections in pp collisions at $\sqrt{s} = 7$ TeV using the anti-k_{T} algorithm with $R = 0.2$ (0.3, 0.4, and 0.6) within $|\eta^{\mathrm{jet}}| \leq 0.7$ ($|\eta^{\mathrm{jet}}| \leq 0.6$, $|\eta^{\mathrm{jet}}| \leq 0.5$, and $|\eta^{\mathrm{jet}}| \leq 0.3$).

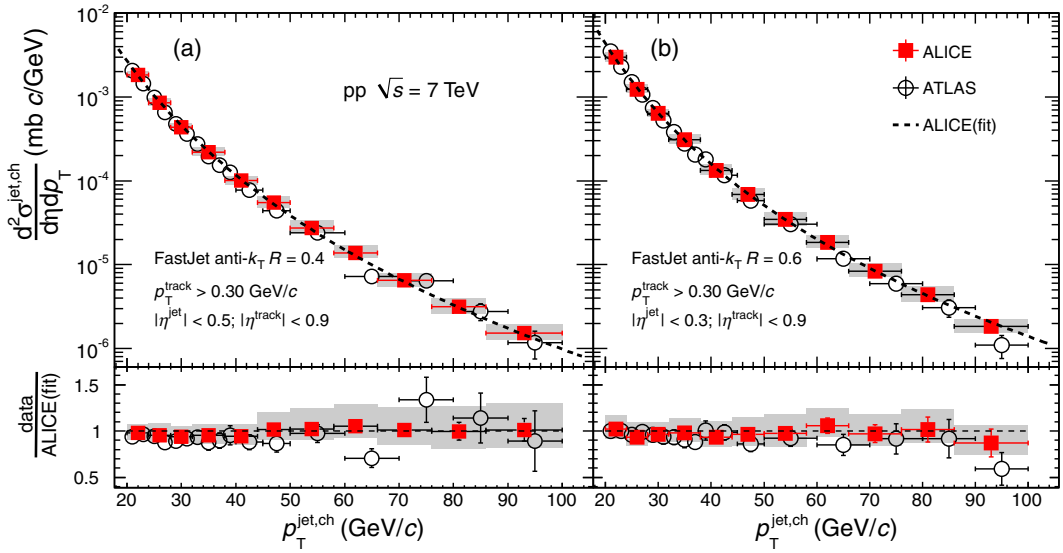

FIG. 4 (color online). Top panels: Comparison of the charged jet cross section in the ALICE and the ATLAS [12] experiments in pp collisions at $\sqrt{s} = 7$ TeV. Statistical and systematic uncertainties are shown separately for ALICE data points, the gray bands indicating the systematic uncertainties, while for the ATLAS data points, the error bars show the statistical and systematic uncertainties summed in quadrature. The dotted line represents a Tsallis fit used to parametrize the ALICE data. Bottom panels: The ratio of the ALICE and ATLAS charged jet spectrum to the parametrized ALICE data. Note that the labels in the figures correspond to the ALICE measurements (see text for details).

algorithms. For larger $p_T^{jet,ch}$ SISCone and k_T algorithms agree within errors with the anti-k_T algorithm. These observations are in good agreement with that obtained using PYTHIA Perugia-0 simulation (not shown).

The anti-k_T algorithm initiates particle clustering around the highest p_T particles of an event. In contrast, the k_T algorithm initiates jet finding by clustering particles with the lowest momenta. It is thus rather sensitive to events with a large, fluctuating density of low momentum particles as produced in A–A collisions. The anti-k_T algorithm does not exhibit such sensitivity and is thus favored for studies of jet production in A–A collisions. Since there are no large differences observed between the spectra obtained with the three jet finders discussed above, and considering the fact that the results of this work will be used as a reference for similar measurements in A–A and p–A collisions, the remainder of the analyses presented in this work are performed with the anti-k_T algorithm exclusively.

B. Charged jet cross section

Figure 3 presents the fully corrected inclusive charged jet cross section measured in pp collisions at $\sqrt{s} = 7$ TeV

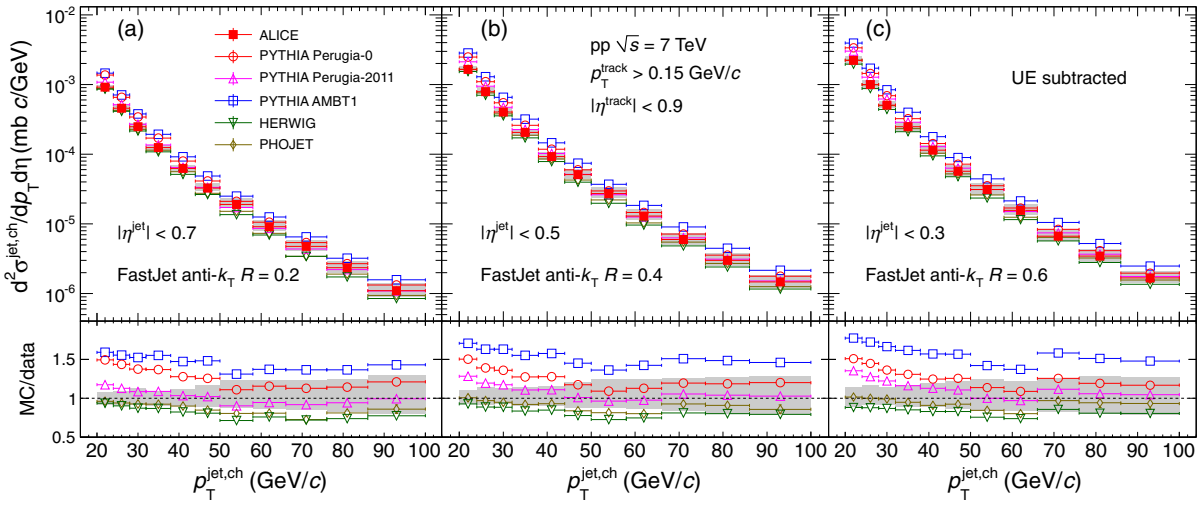

FIG. 5 (color online). Top panels: Charged jet cross sections measured in the ALICE experiment in pp collisions at $\sqrt{s} = 7$ TeV compared to several MC generators: PYTHIA AMBT1, PYTHIA Perugia-0 tune, PYTHIA Perugia-2011 tune, HERWIG, and PHOJET. Bottom panels: Ratios MC/Data. Shaded bands show quadratic sum of statistical and systematic uncertainties on the data drawn at unity.

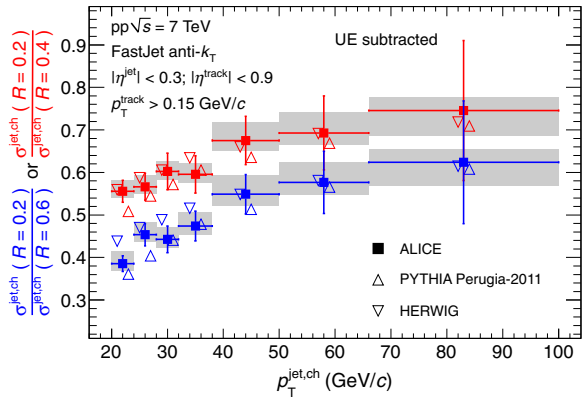

FIG. 6 (color online). Ratios of jet cross sections for charged jets reconstructed using anti-k_T algorithm with resolution parameters 0.2 and 0.4 and 0.2 and 0.6. The jet acceptance is restricted to $|\eta^{jet}| \leq 0.3$. The ratios in data are compared to PYTHIA Perugia-2011 and HERWIG simulations.

using the anti-$k_T$jet finder. Corrections for the detector response and instrumental effects are carried out using the Bayesian unfolding method presented in Sec. VI B. The distributions are also corrected for UE contamination on an event-by-event basis according to the method described in Sec. VI D. Inclusive charged jet cross sections are reported for resolution parameter values $R = 0.2$, 0.3, 0.4 and 0.6, and limited to pseudorapidity ranges $|\eta| < (0.9 - R)$ in order to avoid losses due to partially reconstructed jets at the edge of the pseudorapidity acceptance. Statistical uncertainties are displayed as vertical error bars. Individual sources of systematic uncertainties are p_T dependent. In Fig. 3 as well as in all other figures the data points are placed at the bin center along the abscissa and the horizontal error bars indicate the bin width while the vertical error bars indicate the statistical uncertainties. The total systematic uncertainties are obtained as a quadratic sum of individual systematic uncertainties, as described in Sec. VII, and are shown as shaded bands around the data points in Fig. 3 as well as in all other figures.

The measured charged jet cross sections are compared to those reported by the ATLAS experiment [12] at $R = 0.4$ and 0.6 in Fig. 4. The ATLAS charged jets are measured in the rapidity $|y| \leq 0.5$ at both $R = 0.4$ and 0.6, using charged tracks with $p_T \geq 0.3$ GeV/c without underlying event subtraction. The ALICE therefore also uses the same track p_T selection without underlying event subtraction unlike Fig. 3. To quantify the level of agreement between the ALICE and ATLAS jet cross section measurements, the ALICE data are fitted with a modified Tsallis [70,71] distribution ($f(p_T) = a \cdot (1 + \frac{p_T}{b})^{-c}$). The Tsallis fits are shown as dotted black curves in the top panels of Fig. 4. The χ^2/dof of the fits are 2.97/8 and 4.27/8 for $R = 0.4$ and 0.6, respectively. The bottom panels of Fig. 4 show the ratios of the ALICE and ATLAS data points to the fit function. The gray bands represent the systematic uncertainties on ALICE data points. Despite fluctuations in the high p_T range of the ATLAS data, both data sets are in excellent agreement.

In the top panels of Fig. 5, the measured charged jet cross sections are compared to predictions from PYTHIA (tunes Perugia-0, Perugia-2011, and AMBT1), PHOJET, and HERWIG for $R = 0.2$, 0.4 and 0.6. The ratios of the MC simulations to measured data are shown in the bottom

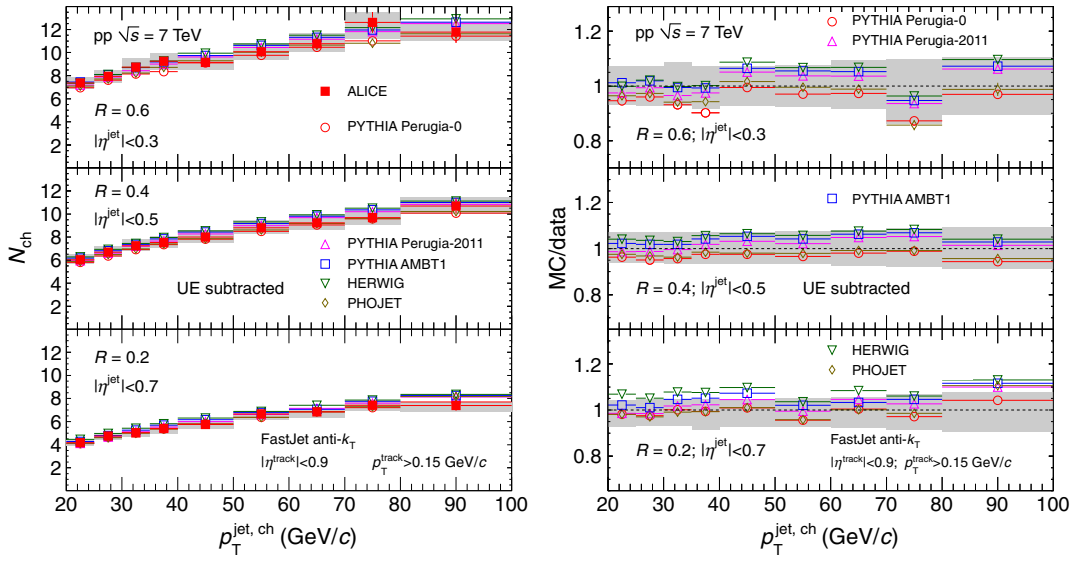

FIG. 7 (color online). Left panel: Mean charged particle multiplicity in the leading charged jet as a function of jet p_T compared to MC models for pp collisions at $\sqrt{s} = 7$ TeV for various jet resolution parameters [$R = 0.6$ (left top), $R = 0.4$ (left middle) and $R = 0.2$ (left bottom)]. UE contributions are subtracted from both data and MC. Right panel: Ratios MC/data. Shaded bands show the quadratic sum of statistical and systematic uncertainties on the data drawn at unity.

panels of Fig. 5. In the high p_T range, PYTHIA Perugia-2011 describes the data best, while in the low p_T range data is best described by HERWIG and PHOJET. All PYTHIA tunes systematically overestimate the measured data in the low transverse momentum range and the discrepancy increases with increasing cone size. The worst discrepancy with the data is observed for the PYTHIA tune AMBT1, which overestimates the data by factors ranging from 25% to 75% over the studied p_T range for $R = 0.2$. The disagreement grows with increasing resolution parameter, and is worst for $R = 0.6$.

Figure 6 shows the ratios of cross sections for jets with resolution parameters $R = 0.2$, $R = 0.4$ and $R = 0.2$, $R = 0.6$. The ratio of jet spectra [15] is sensitive to the collimation of particles around the jet axis and serves as an indirect measure of the jet structure used particularly in A–A collisions [72], where large background fluctuations greatly complicate jet shape studies. In order to compare the ratios within the same jet pseudorapidity range, the ratios are studied within $|\eta| < 0.3$, which coincides with the fiducial jet acceptance for the largest resolution parameter studied ($R = 0.6$). To avoid statistical correlations between the numerator and denominator, disjoint subsets of the data are used. The measured ratios are also compared to those from PYTHIA Perugia-2011 and HERWIG simulations. The measured ratios confirm the expected trend of increased collimation with increasing transverse momentum of jets, corroborated also by the simulation results. At high p_T (>30 GeV/c), both PYTHIA and HERWIG are in good agreement with the data within uncertainties. However, at low p_T (<30 GeV/c), PYTHIA tends to underpredict the data for both the ratios whereas HERWIG tends to overpredict the data for the ratio $\sigma^{\mathrm{jet,ch}}(R = 0.2)/\sigma^{\mathrm{jet,ch}}$ ($R = 0.6$).

C. Charged particle multiplicity in the leading jet

The corrected mean charged particle multiplicity distributions $\langle N_{\mathrm{ch}} \rangle$ in the leading jet are shown in Fig. 7 (left panel) as a function of jet p_T for $R = 0.2$, 0.4, and 0.6. The

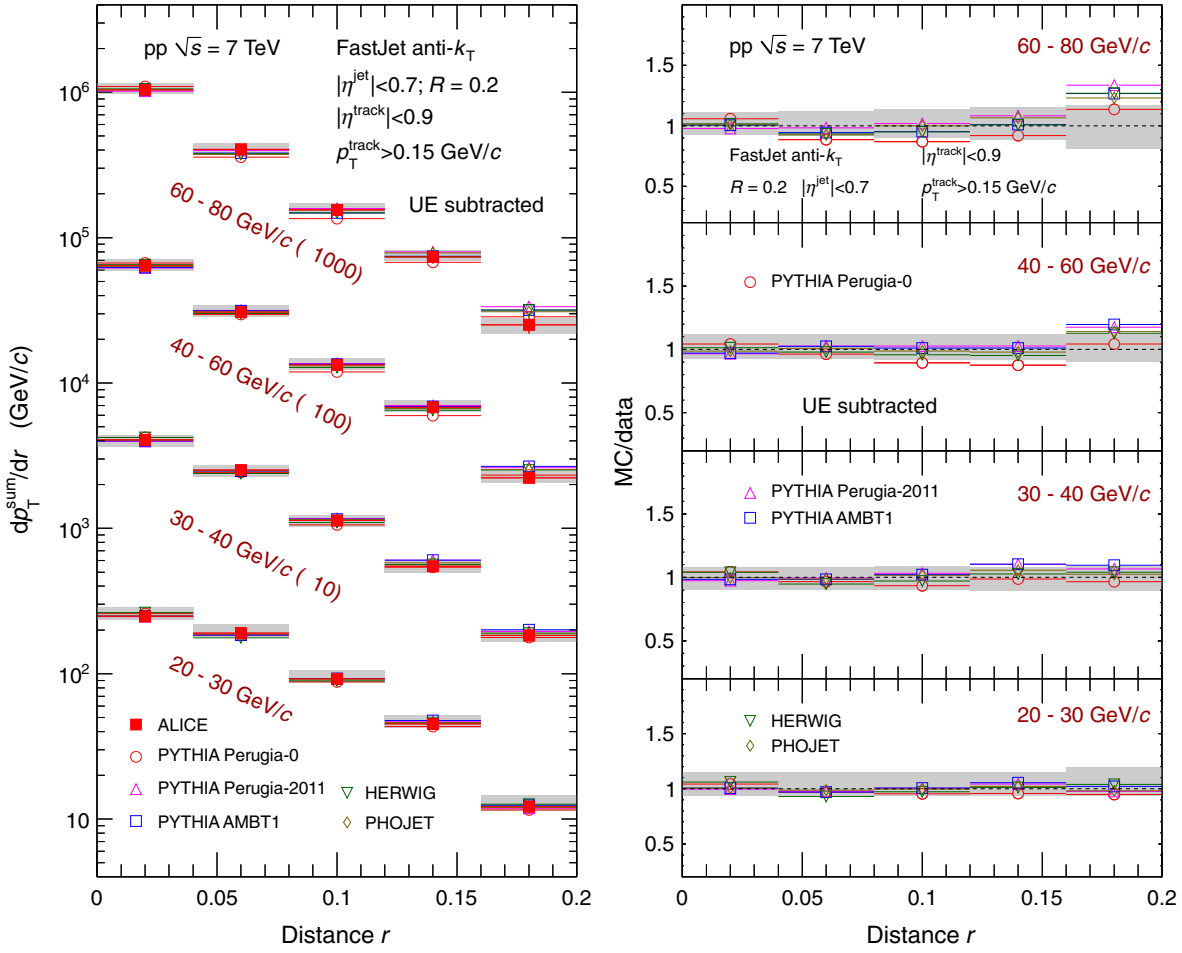

FIG. 8 (color online). Left panel: Radial distributions of p_T density as a function of radial distance 'r' from the jet direction for leading charged jets reconstructed with resolution parameter $R = 0.2$ for selected jet p_T ranges in pp collisions at $\sqrt{s} = 7$ TeV. Measured distributions are compared to MC model calculations. UE contributions are subtracted from both data and MC. Right panel: Ratios MC/data. Shaded bands show the quadratic sum of statistical and systematic uncertainties of the data drawn at unity.

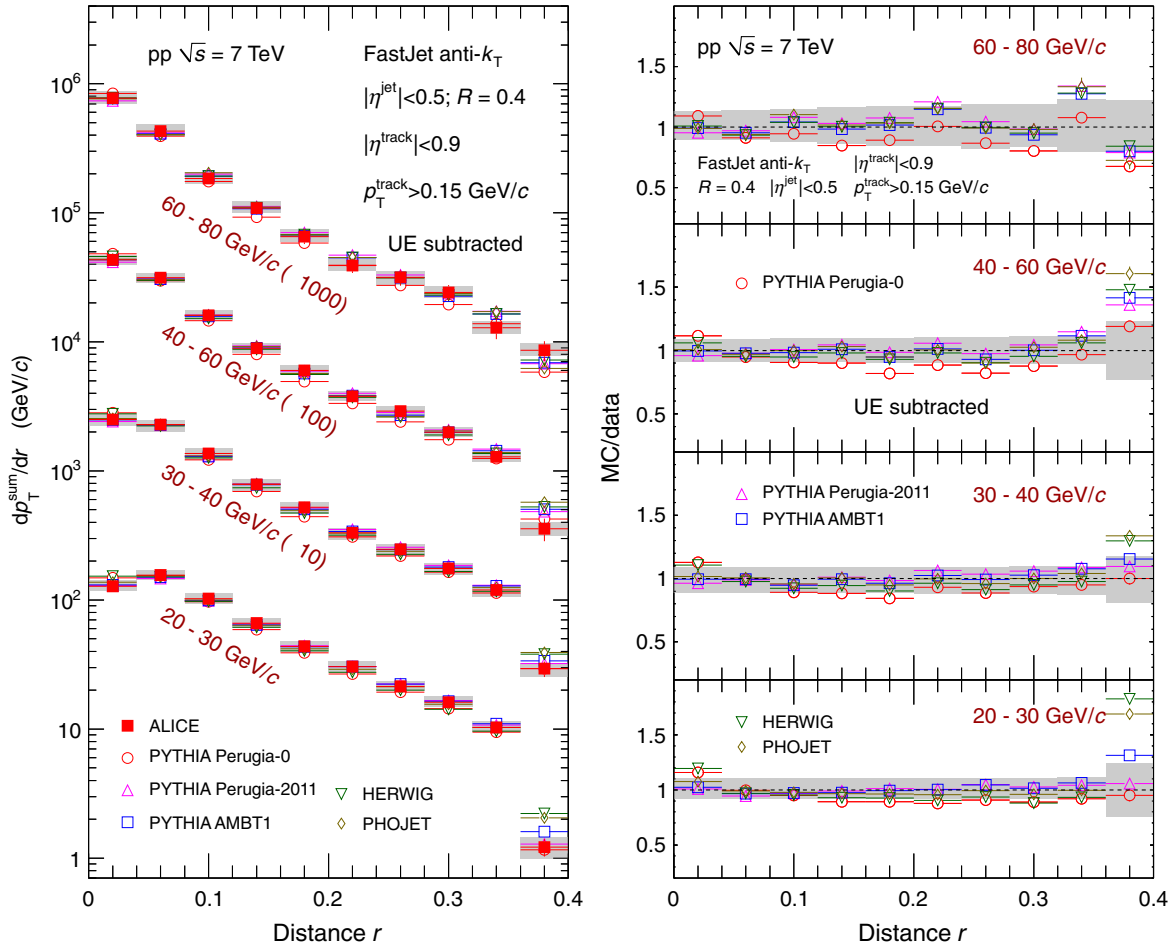

FIG. 9 (color online). Same as Fig. 8 for a resolution parameter $R = 0.4$.

$\langle N_{ch} \rangle$ rises monotonically with increasing jet p_T as well as with increasing R. These results are in qualitative agreement with those reported by the CDF [17] Collaboration and more recently by the CMS [21] Collaboration based on slightly different kinematic track cuts.

In the left panel of Fig. 7, the measurements are compared to predictions by the MC models PYTHIA (tunes Perugia-0, Perugia-2011, AMBT1), PHOJET, and HERWIG. Ratios of the predictions to the data are displayed in the right panel. The model predictions are well within 10% of the measured data with largest deviations of ~15% at $R = 0.6$ and 0.2 towards large jet p_T. The PYTHIA tune Perugia-0 tends to systematically underestimate the measured particle multiplicities particularly at the largest R for smaller jet momentum, whereas HERWIG tends to overpredict the data at smaller R. An overall agreement between the data and MC predictions is found to be best with the Perugia-2011 tune and PHOJET.

D. Transverse momentum density distributions within the leading jet

The left panels of Figs. 8, 9, and 10 show leading jets average p_T density radial distributions $\langle dp_T^{sum}/dr \rangle$ measured with resolution parameters $R = 0.2$, 0.4, and 0.6, respectively. The distributions are plotted separately for jets in the p_T intervals 20–30, 30–40, 40–60, and 60–80 GeV/c. The latter three distributions are scaled by factors of 10, 100, and 1000, respectively, for clarity. The transverse momentum density is largest near the jet axis and decreases approximately exponentially with increasing r. Densities are largest at the highest jet p_T where they are also found to have the steepest dependence on r. This indicates that high p_T jets are on average more collimated than low p_T jets as already hinted in Fig. 6.

The measured distributions are compared to predictions with MC models. The right panels of Figs. 8, 9, and 10 display ratios of the model calculations to measured data. The MC models qualitatively reproduce the magnitude of the measured densities as well as their radial dependence. The agreement between the MC model calculations and data is better at smaller $R(= 0.2)$. At $R = 0.4$ and 0.6 HERWIG and Perugia-0 tune of PYTHIA tend to underpredict the measured transverse momentum density except at small r for the two lowest jet p_T bins. The excess over the data for the smallest r and the slope of the ratio of simulations to data observed for $R = 0.6$ indicates stronger

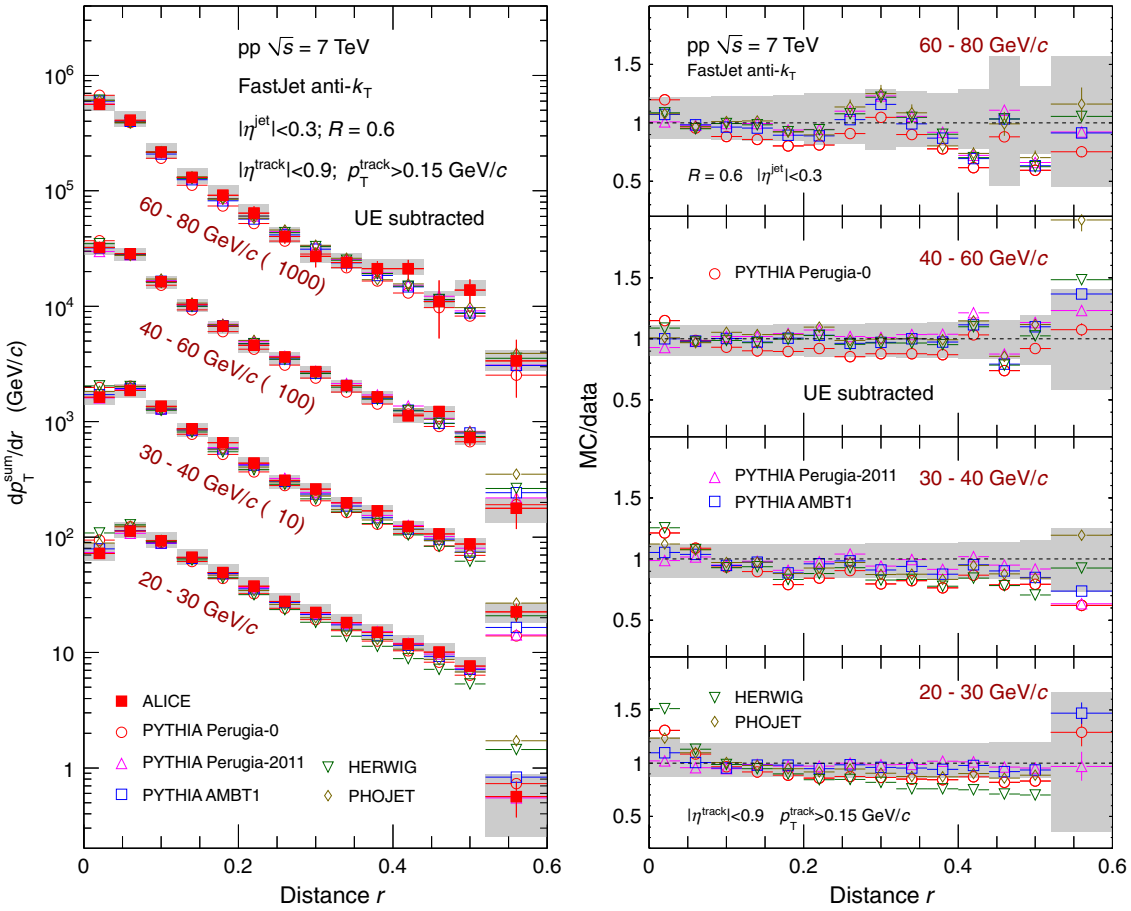

FIG. 10 (color online). Same as Fig. 8 for a resolution parameter $R = 0.6$.

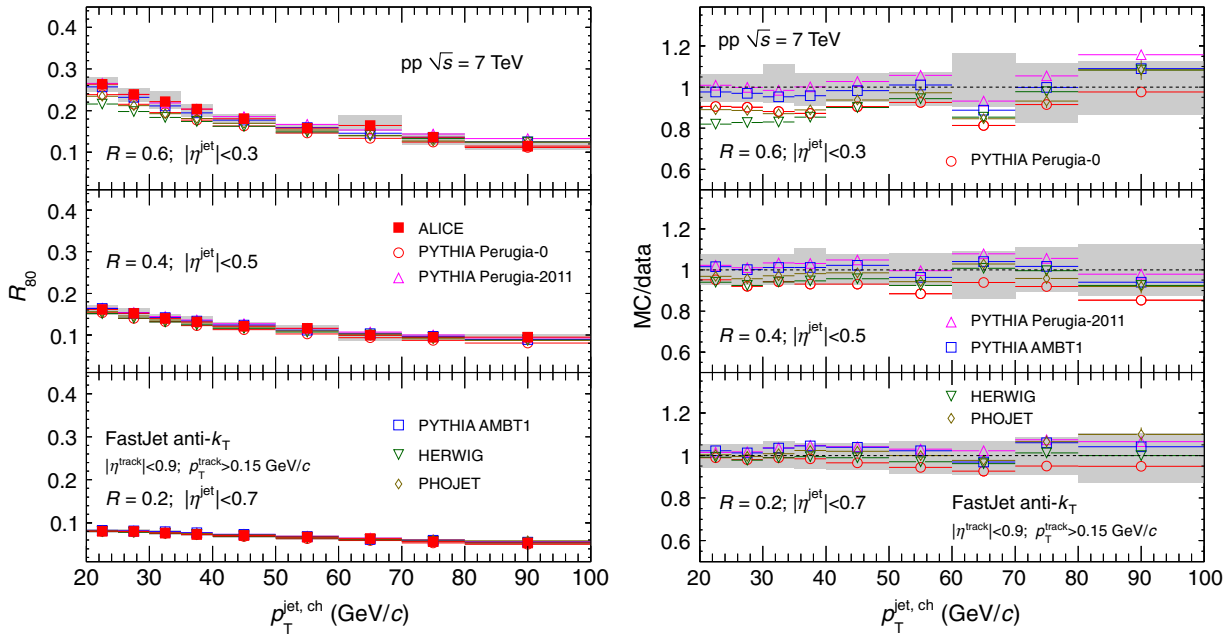

FIG. 11 (color online). Left panel: Distributions of average radius $\langle R_{80} \rangle$ containing 80% of the p_T with respect to the total reconstructed jet p_T as a function of jet p_T compared to MC models for pp collisions at $\sqrt{s} = 7$ TeV for various jet resolution parameters [$R = 0.6$ (left top), $R = 0.4$ (left middle) and $R = 0.2$ (left bottom)]. Right panel: Ratios MC/data. Shaded bands show quadratic sum of the statistical and systematic uncertainties of the data drawn at unity.

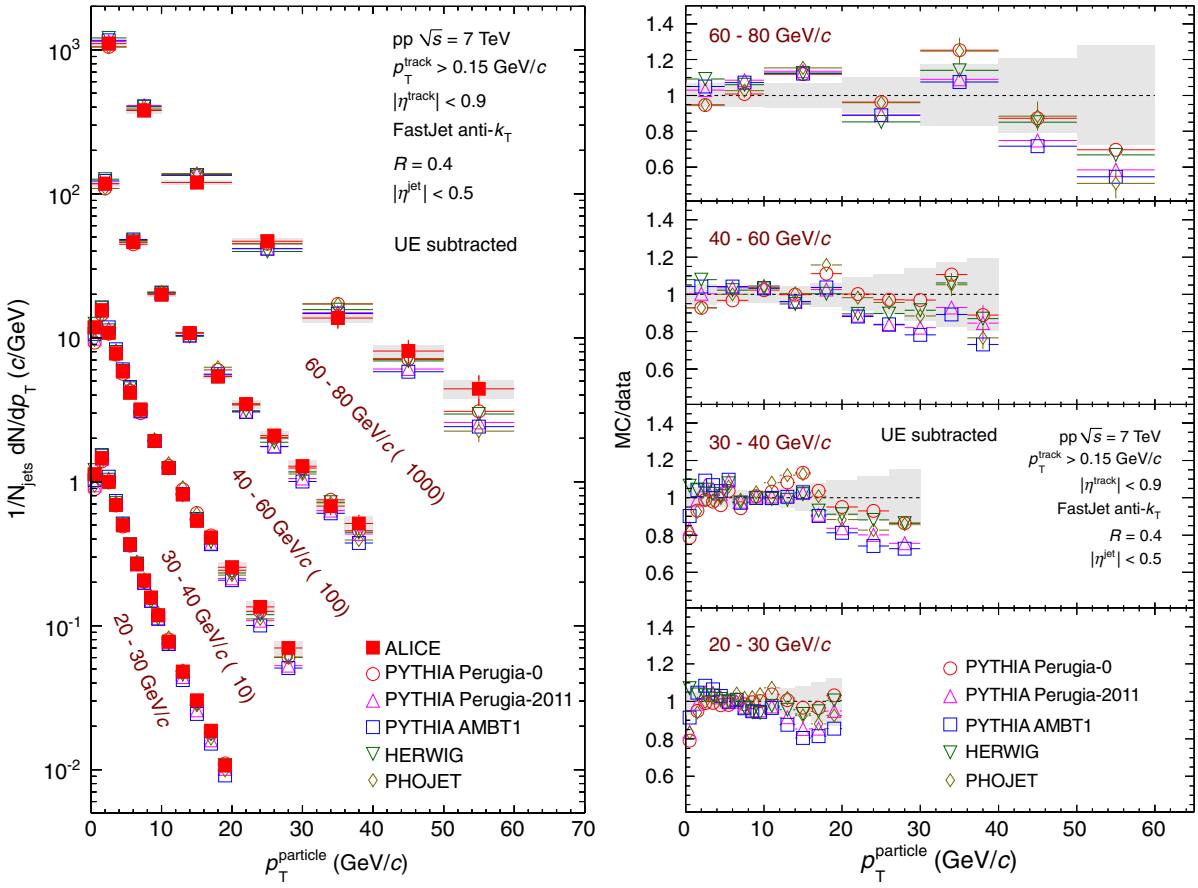

FIG. 12 (color online). Left panel: Charged particle p_T spectra dN/dp_T in leading jets for different bins in jet transverse momentum, compared to simulations. For simulations and data, the UE contribution is subtracted. Right panel: Ratio of simulations to data. The shaded band indicates the quadratic sum of statistical and systematic uncertainties on the data.

jet collimation for low p_T jets than observed in the data. This observation is consistent with the discrepancy of the Herwig model to the measured cross section ratio discussed in Sec. VIII B (see also Fig. 6). In the last bin of Figs. 9, and 10 (right panel), large deviations of MC models (PHOJET and HERWIG) from the data are found, whereas good agreement is observed when data and simulations are not corrected for the UE contribution (see Appendix A). This indicates that the UE is underestimated by these models, as reported in [65] for PHOJET and in [63] for HERWIG simulations of the UE density of charged and neutral particles with $p_T > 0.5$ GeV/c.

E. Leading charged jet size

The left panel of Fig. 11 displays measured distributions of the average radius, $\langle R_{80}\rangle$, containing 80% of the total jet p_T observed in jet cones with $R = 0.2$, 0.4, and 0.6. The distributions are corrected using the bin-by-bin method described in Sec. VI A to account for instrumental effects. No corrections are applied for UE contributions, which are estimated to have a negligible effects on measured $\langle R_{80}\rangle$ values. Jet widths are largest at the lowest measured p_T and decrease monotonically with increasing p_T, indicating that high p_T jets are more collimated than low p_T jets (as observed in Figs. 6, 8, 9, and 10) in a similar way as predicted by various MC models and in qualitative agreement with prior measurement by the CDF [17] Collaboration.

Figure 11 also displays $\langle R_{80}\rangle$ distributions predicted by PYTHIA (tunes Perugia-0, Perugia-2011, AMBT1), PHOJET, and HERWIG. All five models qualitatively reproduce the observed magnitude and p_T dependence of $\langle R_{80}\rangle$ at $R = 0.2$ and 0.4. However, at $R = 0.6$, HERWIG, PHOJET, and PYTHIA Perugia-0 tune systematically underpredict the data at low p_T. The PYTHIA tunes Perugia-2011 and AMBT1 are in best agreement with the measured values.

F. Jet fragmentation

The left panels of Figs. 12, 13, and 14 present the measured p_T spectra F^{p_T} and scaled p_T spectra F^z and F^ξ of charged particles in leading charged jets reconstructed with a resolution parameter $R = 0.4$. The data are corrected for instrumental effects, UE background, and

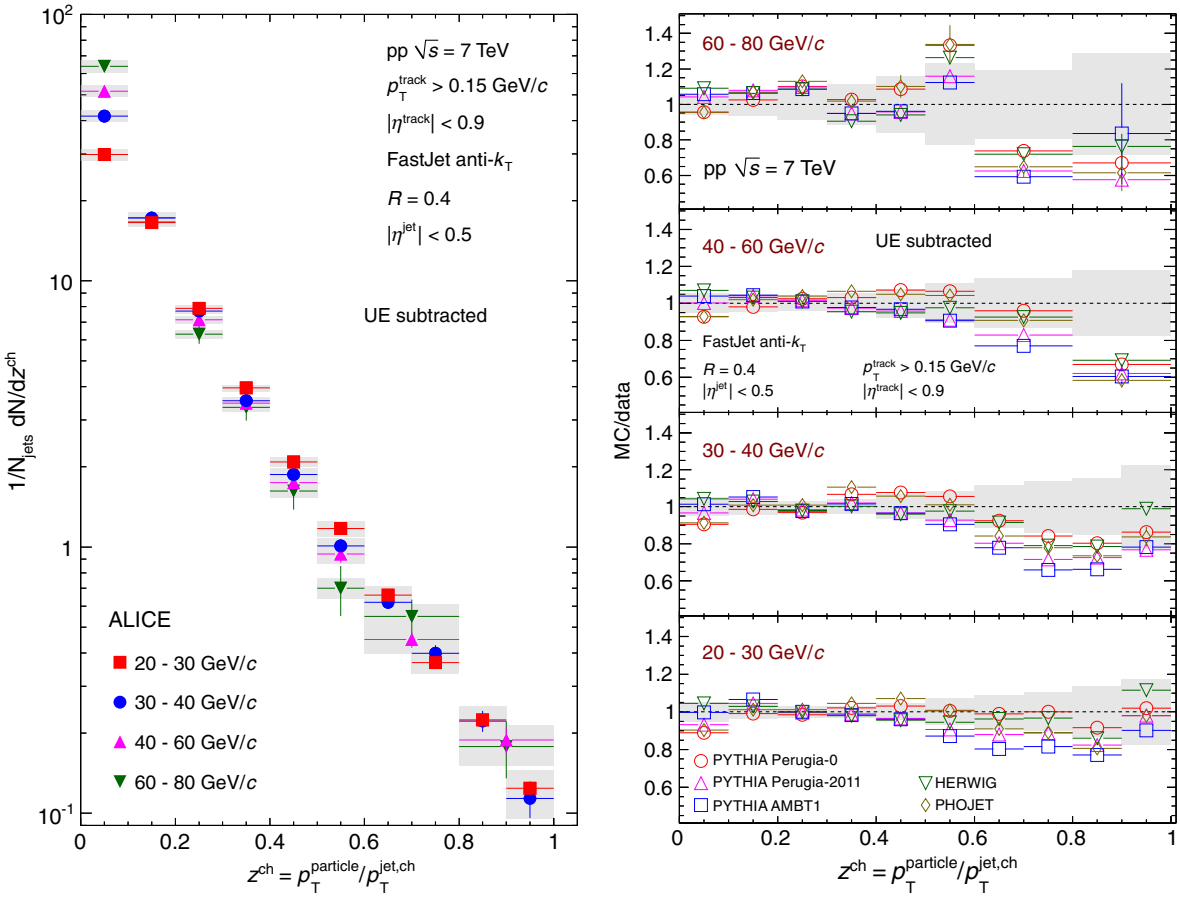

FIG. 13 (color online). Left panel: Charged particle scaled p_T spectra dN/dz^{ch} in leading jets for different bins in jet transverse momentum. Right panel: Ratio of simulations to data. The shaded band indicates the quadratic sum of statistical and systematic uncertainties on the data. UE contributions are subtracted from both data and simulations.

contamination from secondary particles. Systematic uncertainties, indicated by the shaded bands, include the detector response, UE subtraction, correction for secondaries and event generator dependence.

The particle momentum distributions F^{p_T} are shown for four bins in jet transverse momentum: 20–30, 30–40, 40–60, and 60–80 GeV/c. The latter three are scaled by factors of 10, 100, and 1000, respectively, for clarity. The p_T spectra of the jet constituents span 2–3 orders of magnitude. The slopes are steepest for the lowest p_T jets and progressively flatter with increasing jet p_T. This dependence is essentially driven by the jet energy scale, as illustrated in Fig. 13, which displays fragmentation distributions F^z for jets in the same four jet momentum ranges. For $z^{ch} > 0.1$ all measured distributions are consistent within uncertainties, indicating a scaling of charged jet fragmentation with charged jet transverse momentum.

The fragmentation distributions F^ξ, shown in Fig. 14, resolve in more detail the differences observed for small values of z^{ch}. For small values of $\xi^{ch} \lesssim 2$, the distributions exhibit the approximate scaling already seen for F^z, whereas at higher ξ^{ch}, corresponding to small z^{ch}, a pronounced maximum ("hump-backed plateau") is observed, indicating the suppression of low momentum particle production by QCD coherence [47,48]. With increasing jet transverse momentum, the area of the distributions increases, showing the rise of particle multiplicity in jets (as observed in Fig. 7), and the maximum shifts to higher values of ξ^{ch}. This observation is in qualitative agreement with full di-jet fragmentation functions measured in $p\bar{p}$ collisions at $\sqrt{s} = 1.8$ TeV [23] and with expectations from QCD calculations based on the modified leading logarithmic approximation (MLLA) [73].

The measured fragmentation distributions are compared to calculations obtained from the HERWIG [28,29], PHOJET [30] and PYTHIA [27] event generators and the ratios of the calculated MC distributions to measured distributions are shown in the right panels of Figs. 12, 13, and 14. The UE contributions to MC events are estimated and subtracted using perpendicular cones pointing into the event transverse region as described in Sec. VI D. At high particle transverse momenta and high z^{ch}, the data and simulations agree within uncertainties, except for the two lowest jet p_T bins, where the measured yield seems to be

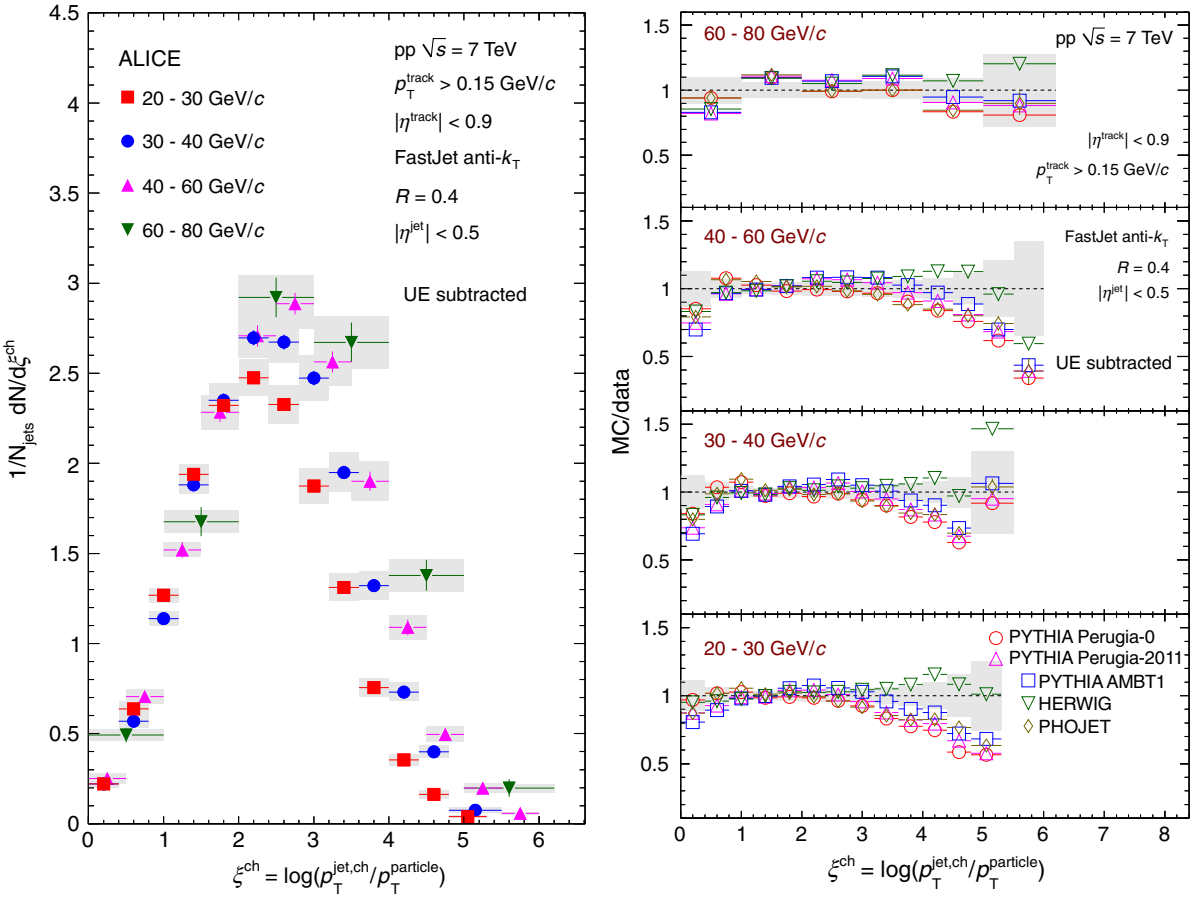

FIG. 14 (color online). Left panel: Charged particle scaled p_{T} spectra $\mathrm{d}N/\mathrm{d}\xi^{\mathrm{ch}}$ in leading jets for different bins in jet transverse momentum. Right panel: Ratio of simulations to data. The shaded band indicates the quadratic sum of statistical and systematic uncertainties on the data. UE contributions are subtracted from both data and simulations.

systematically higher than the simulations with PYTHIA tunes Perugia-2011 and AMBT1 for $z^{\mathrm{ch}} > 0.6$. In the low-momentum/high-ξ^{ch} region, the measured yield is systematically larger than the ones produced by the PYTHIA and PHOJET simulations. To investigate the discrepancy at low particle momentum, data and simulations are also compared without subtraction of the UE (see Appendix A). In this case, the excess of low momentum constituents in data over PYTHIA simulations is still significant, however reduced in magnitude and comparable to other measurements at higher constituent momenta [12]. It is thus concluded that in the PYTHIA tunes investigated in this work, the UE contribution to the low momentum particle yield is overestimated relative to the contribution from hard parton fragmentation. The data at low p_{T} are best described by the HERWIG event generator, which hints to a sensitivity of the low momentum fragmentation to the details of the parton shower model in the simulations.

IX. SUMMARY AND CONCLUSION

In summary, we reported measurements of the inclusive charged particle jet cross section, jet fragmentation and jet shapes at midrapidity in pp collisions at $\sqrt{s} = 7$ TeV using the ALICE detector at the LHC.

Jets were reconstructed with infrared and collinear safe jet finding algorithms, k_{T}, anti-k_{T} and a seedless infrared safe iterative cone based algorithm, SISCone. As the measured inclusive jet spectra did not show any significant dependence on the jet algorithm used, all observables discussed throughout the paper were based on jets reconstructed with the anti-k_{T} sequential recombination algorithm, commonly utilized in the LHC community. In order to gain as much information as possible, the anti-k_{T} algorithm was run with several resolution parameters R ranging from 0.2 to 0.6.

The inclusive charged jet cross section was measured in the $p_{\mathrm{T}}^{\mathrm{jet,ch}}$ interval from 20 to 100 GeV/c and found to be consistent with the ATLAS measurement at the same collision energy. The ratios of jet cross sections for resolution parameter $R = 0.2$ over $R = 0.4$ and 0.6, respectively, are found to increase with increasing p_{T} of jets, pointing toward an increasing collimation of particles in jets around the jet axis. This finding, expected by pQCD calculations, is corroborated by a detailed study of $\langle R_{80} \rangle$

variable defined as the average radius containing 80% of total charged jet p_{T}. The p_{T} density is found to be the largest near the jet axis and decreases radially away from the jet axis. This radial decrease is found to be larger for high p_{T} jets which are more collimated. The averaged charged particle multiplicity in jets ($\langle N_{\mathrm{ch}} \rangle$) increases with jet momentum and resolution parameter R. We studied charged particle fragmentation in leading charged jets. The scaled p_{T} spectra of charged particles associated with jets exhibit a pronounced maximum commonly referred to as 'hump-backed plateau' consistent with the suppression of low momentum particle production by QCD coherence. The area of the distribution increases with jet p_{T} and reflects the observed increase of $\langle N_{\mathrm{ch}} \rangle$ discussed above. The observed behavior is in qualitative agreement with MLLA [73] calculations and earlier measurements [23] in $\mathrm{p\bar{p}}$ collisions at the Tevatron ($\sqrt{s} = 1.8$ TeV). The jet fragmentation distributions for the measured jet p_{T} ranges indicate a scaling of charged jet fragmentation with jet p_{T} for $z^{\mathrm{ch}} > 0.1$.

All measured observables were also compared to several MC generators (PYTHIA, PHOJET, HERWIG). None of the generators gives a perfect description of the measured charged jet cross section. PHOJET and most of the PYTHIA tunes used in this work overestimate the cross section. PYTHIA Perugia-2011 agrees reasonably well with the data for intermediate and high charged jet p_{T}, whereas HERWIG reproduces best the cross section at low jet p_{T}. The jet properties are reproduced rather well by the MC generators. The agreement of the calculations with the data for observables $\langle N_{\mathrm{ch}} \rangle$, $\langle R_{80} \rangle$, and radial p_{T} density is typically at the level of 5%–10%. In case of the fragmentation functions, the data are better described by the HERWIG event generator. The high-momentum (low-ξ^{ch}) region is relatively well described by the generators, while for the low momenta (high ξ^{ch}), the measured yield significantly exceeds PHOJET and PYTHIA predictions. We emphasize the relevance of this observation for the choice of a generator based pp reference for future measurements of jet fragmentation in nuclear collisions, where similar effects are predicted as a signature of parton energy loss in the hot and dense strongly-interacting medium.

ACKNOWLEDGMENTS

The ALICE Collaboration would like to thank all its engineers and technicians for their invaluable contributions to the construction of the experiment and the CERN accelerator teams for the outstanding performance of the LHC complex. The ALICE Collaboration gratefully acknowledges the resources and support provided by all Grid centers and the Worldwide LHC Computing Grid (WLCG) Collaboration. The ALICE Collaboration acknowledges the following funding agencies for their support in building and running the ALICE detector: State Committee of Science, World Federation of Scientists (WFS) and Swiss Fonds Kidagan, Armenia, Conselho Nacional de Desenvolvimento Científico e Tecnológico (CNPq), Financiadora de Estudos e Projetos (FINEP), Fundação de Amparo à Pesquisa do Estado de São Paulo (FAPESP); National Natural Science Foundation of China (NSFC), the Chinese Ministry of Education (CMOE) and the Ministry of Science and Technology of China (MSTC); Ministry of Education and Youth of the Czech Republic; Danish Natural Science Research Council, the Carlsberg Foundation and the Danish National Research Foundation; The European Research Council under the European Community's Seventh Framework Programme; Helsinki Institute of Physics and the Academy of Finland; French CNRS-IN2P3, the "Region Pays de Loire," "Region Alsace," "Region Auvergne" and CEA, France; German BMBF and the Helmholtz Association; General Secretariat for Research and Technology, Ministry of Development, Greece; Hungarian OTKA and National Office for Research and Technology (NKTH); Department of Atomic Energy and Department of Science and Technology of the Government of India; Istituto Nazionale di Fisica Nucleare (INFN) and Centro Fermi—Museo Storico della Fisica e Centro Studi e Ricerche "Enrico Fermi", Italy; MEXT Grant-in-Aid for Specially Promoted Research, Japan; Joint Institute for Nuclear Research, Dubna; National Research Foundation of Korea (NRF); CONACYT, DGAPA, México, ALFA-EC and the EPLANET Program (European Particle Physics Latin American Network) Stichting voor Fundamenteel Onderzoek der Materie (FOM) and the Nederlandse Organisatie voor Wetenschappelijk Onderzoek (NWO), Netherlands; Research Council of Norway (NFR); Polish Ministry of Science and Higher Education; National Science Centre, Poland; Ministry of National Education/ Institute for Atomic Physics and CNCS-UEFISCDI—Romania; Ministry of Education and Science of Russian Federation, Russian Academy of Sciences, Russian Federal Agency of Atomic Energy, Russian Federal Agency for Science and Innovations and The Russian Foundation for Basic Research; Ministry of Education of Slovakia; Department of Science and Technology, South Africa; CIEMAT, EELA, Ministerio de Economía y Competitividad (MINECO) of Spain, Xunta de Galicia (Consellería de Educación), CEADEN, Cubaenergía, Cuba, and IAEA (International Atomic Energy Agency); Swedish Research Council (VR) and Knut & Alice Wallenberg Foundation (KAW); Ukraine Ministry of Education and Science; United Kingdom Science and Technology Facilities Council (STFC); The United States Department of Energy, the United States National Science Foundation, the State of Texas, and the State of Ohio; Ministry of Science, Education and Sports of Croatia and Unity through Knowledge Fund, Croatia.

APPENDIX: RESULTS WITHOUT UE SUBTRACTION

The results are presented for charged jet properties including inclusive differential jet cross section, $\langle N_{\mathrm{ch}} \rangle$, $\langle \mathrm{d}p_{\mathrm{T}}^{\mathrm{sum}}/\mathrm{d}r \rangle$, $F^{p_{\mathrm{T}}}$, F^{z} and F^{ξ} without subtraction of UE in comparison to MC generators.

In the top panels of Fig. 15, the measured charged jet cross sections are compared to predictions from PYTHIA (tunes Perugia-0, Perugia-2011, and AMBT1), PHOJET, and HERWIG for $R = 0.4$ and 0.6. The UE is not subtracted for both data and MC. The ratios of the MC simulations to measured data are shown in the bottom panels of Fig. 15.

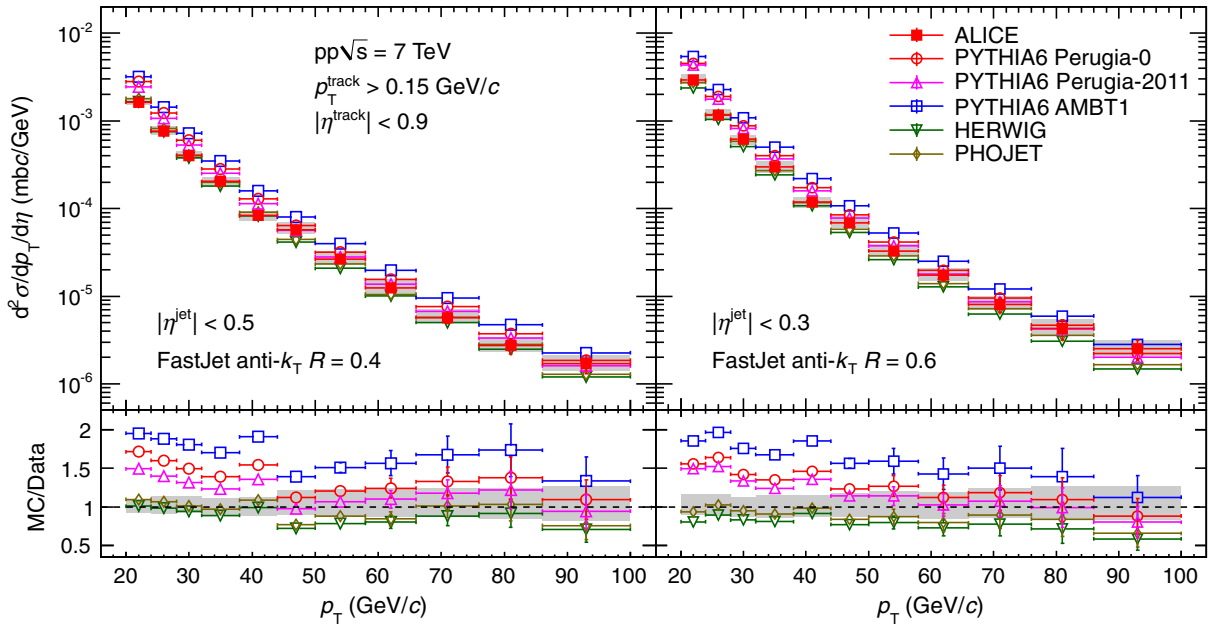

FIG. 15 (color online). Top panels: Charged jet cross sections measured in the ALICE experiment in pp collisions at $\sqrt{s} = 7$ TeV without UE subtraction compared to several MC generators: PYTHIA AMBT1, PYTHIA Perugia-0 tune, PYTHIA Perugia-2011 tune, HERWIG, and PHOJET. Bottom panels: Ratios MC/Data. Shaded bands show quadratic sum of statistical and systematic uncertainties on the data drawn at unity.

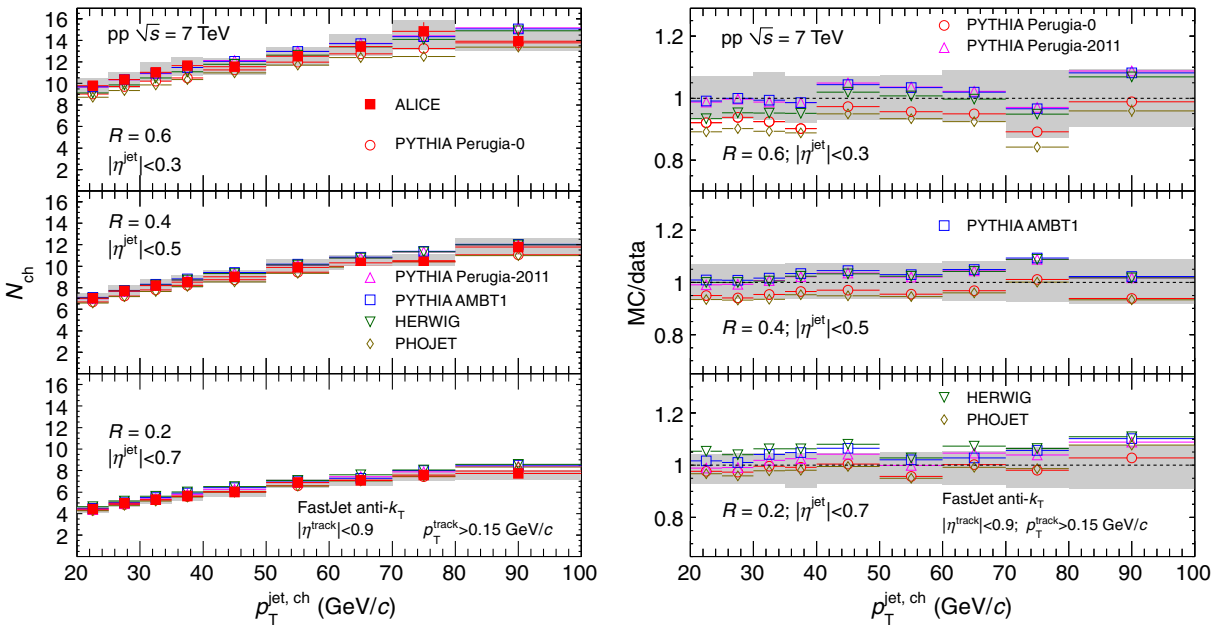

FIG. 16 (color online). Same as Fig. 7 without UE subtraction.

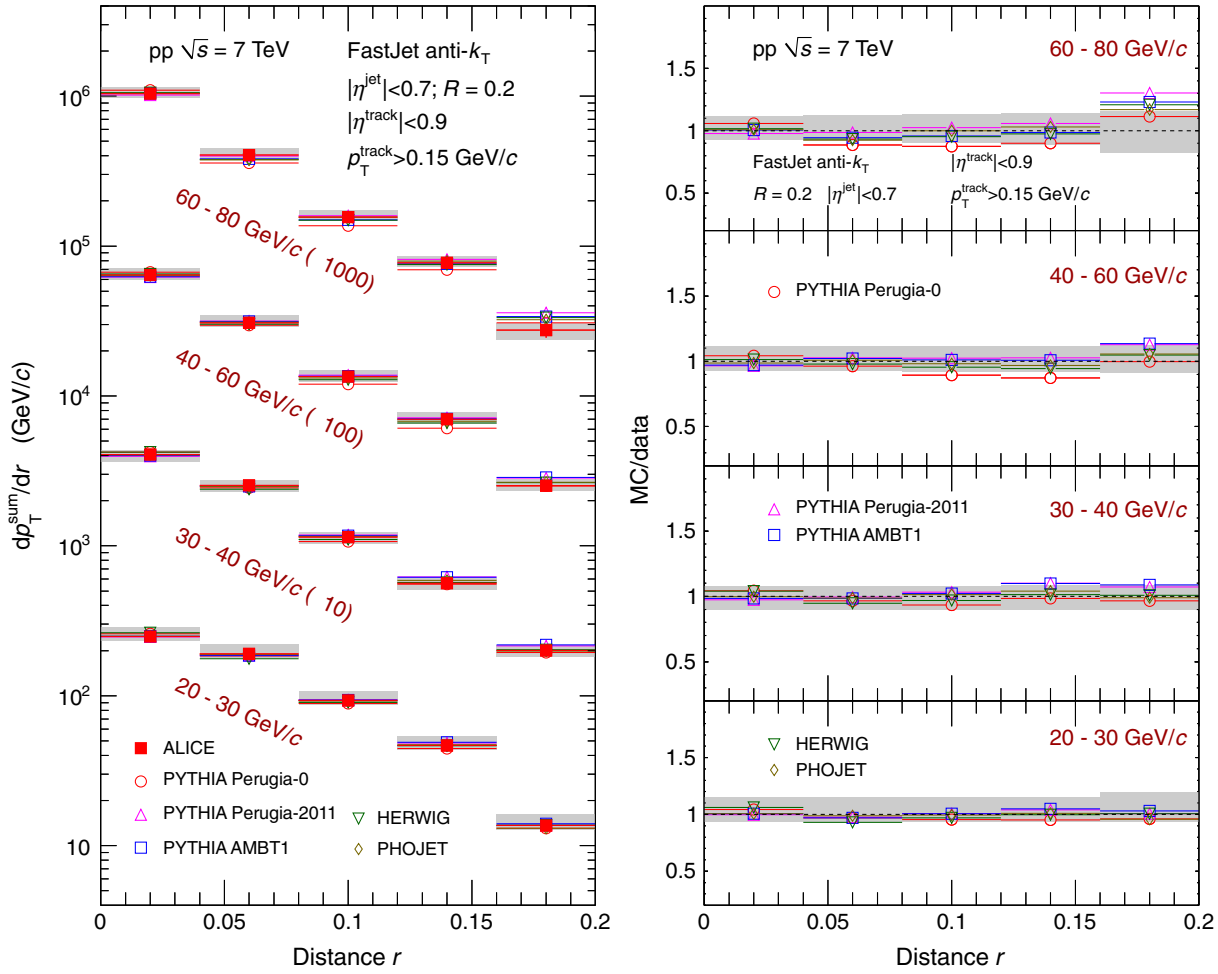

FIG. 17 (color online). Same as Fig. 8 without UE subtraction.

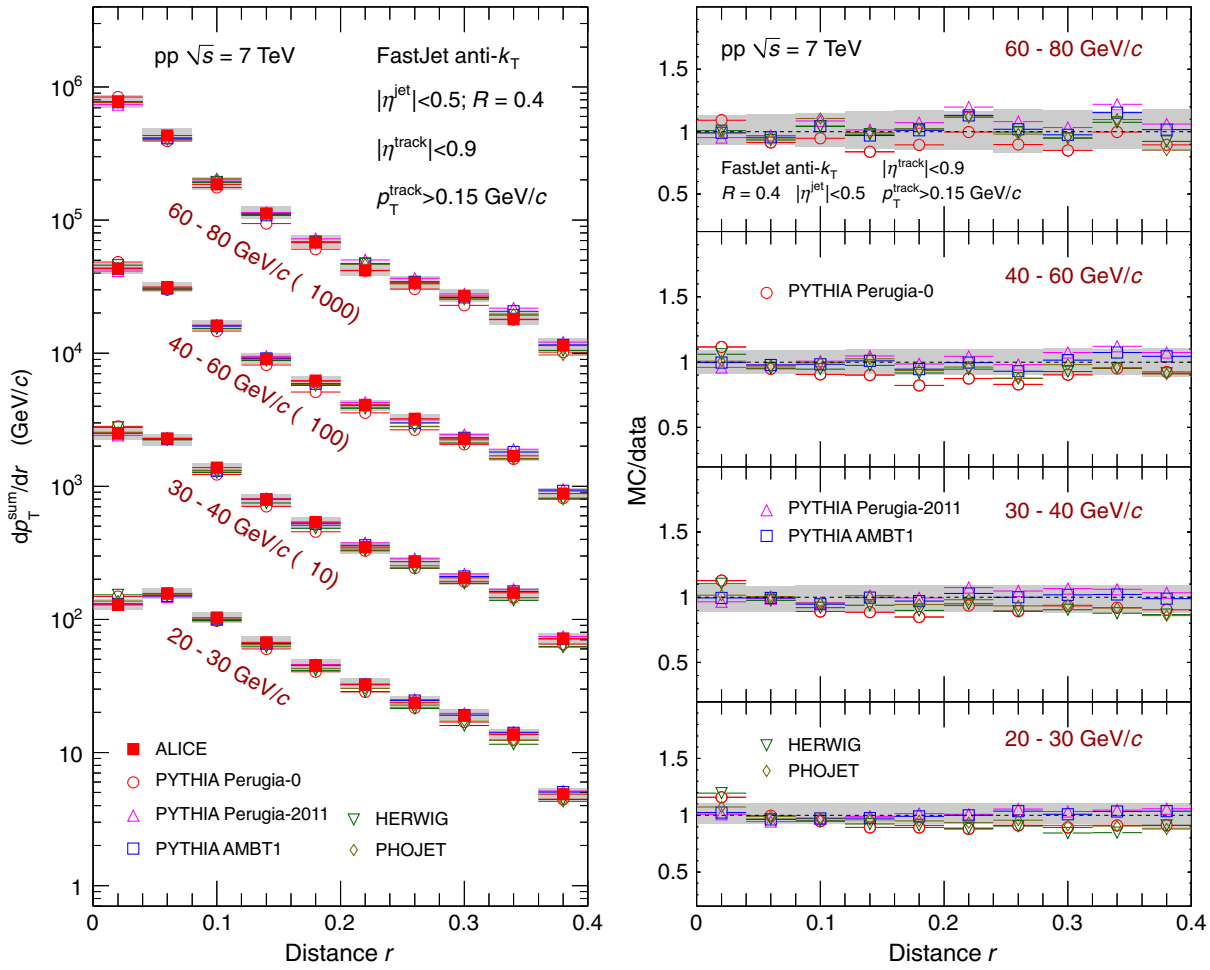

FIG. 18 (color online). Same as Fig. 9 without UE subtraction.

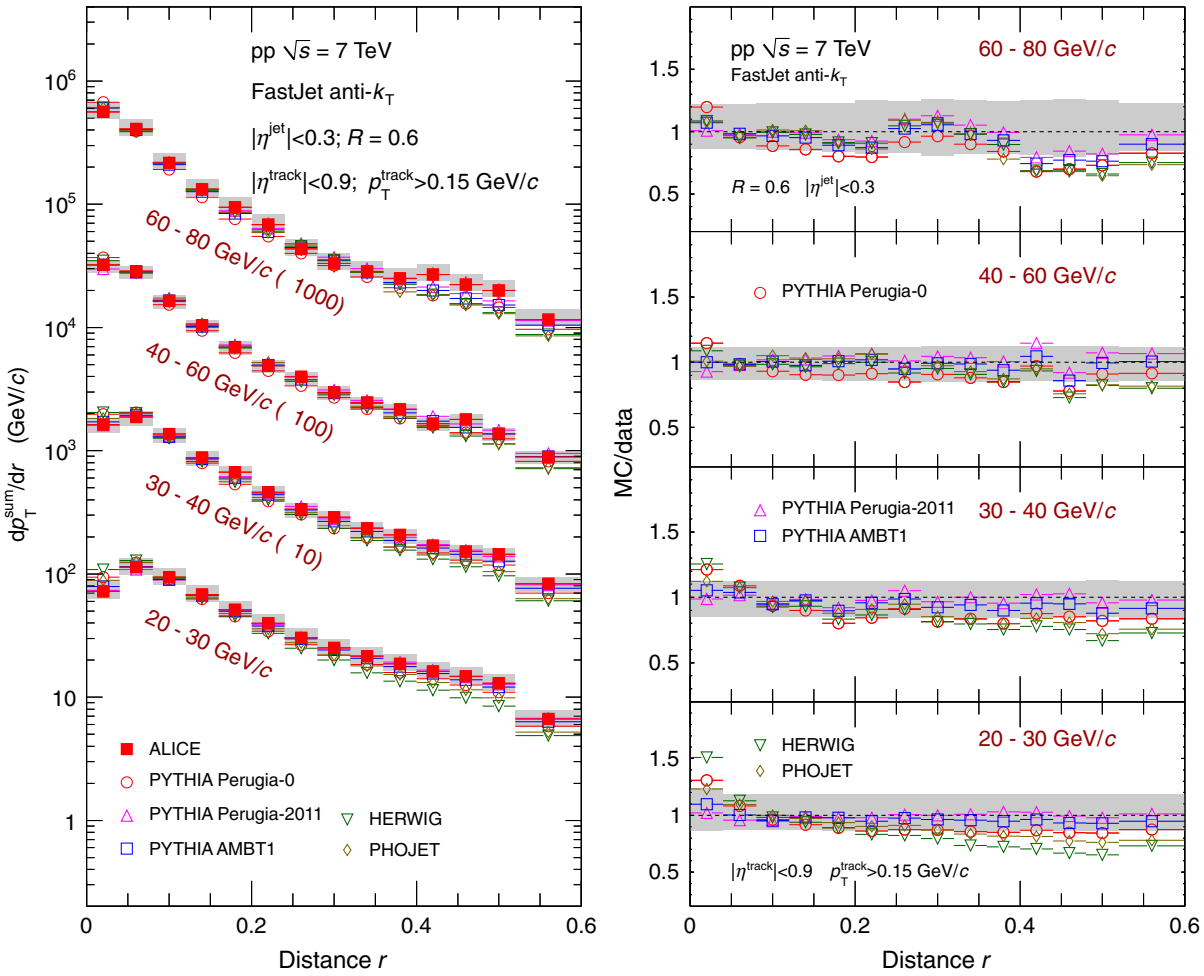

FIG. 19 (color online). Same as Fig. 10 without UE subtraction.

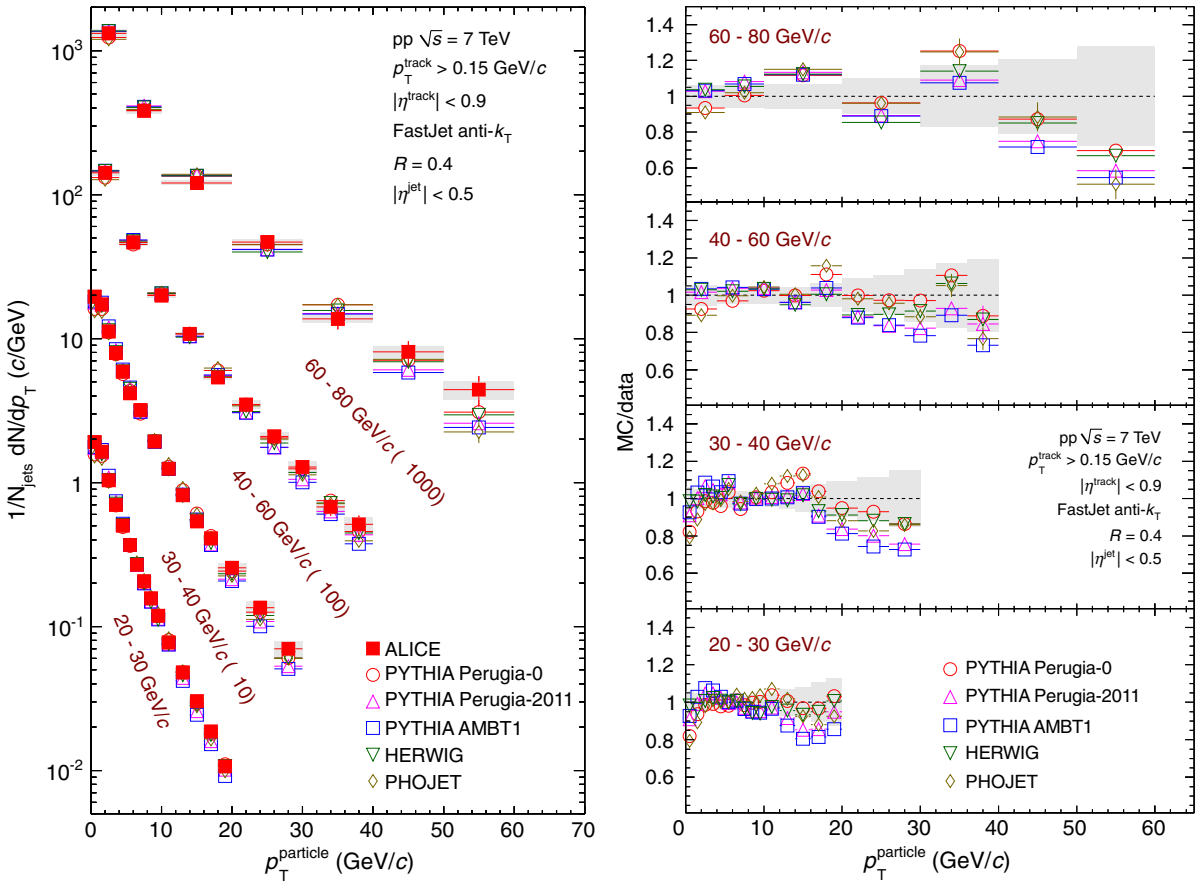

FIG. 20 (color online). Same as Fig. 12 without UE subtraction.

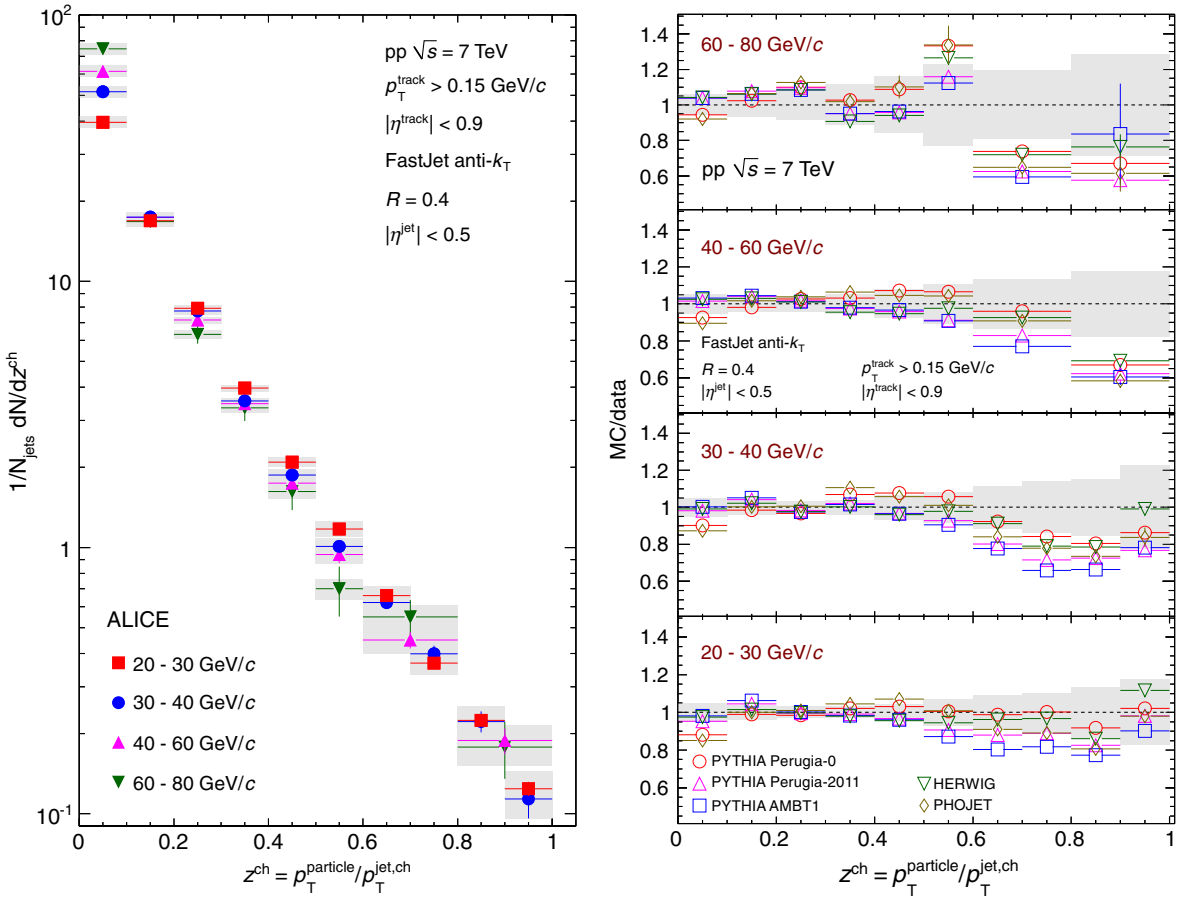

FIG. 21 (color online). Same as Fig. 13 without UE subtraction.

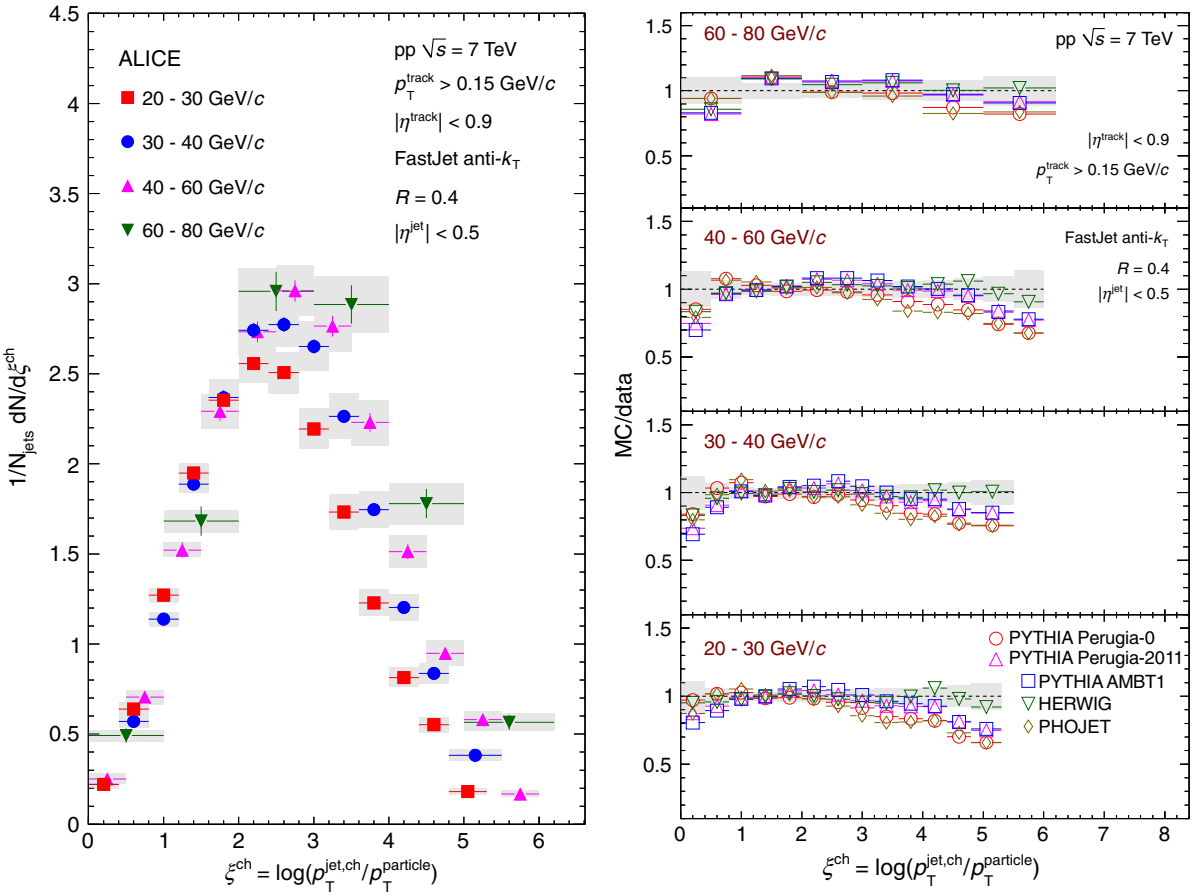

FIG. 22 (color online). Same as Fig. 14 without UE subtraction.

The corrected mean charged particle multiplicity distributions $\langle N_{\mathrm{ch}} \rangle$ in the leading jet are shown in Fig. 16 (left panel) as a function of jet p_{T} for $R = 0.2$, 0.4, and 0.6. The UE is not subtracted for both data and MC. Ratios of the predictions to the data are displayed in the right panel.

The left panels of Figs. 17, 18, and 19 show leading jets average p_{T} density radial distributions $\langle \mathrm{d}p_{\mathrm{T}}^{\mathrm{sum}}/\mathrm{d}r \rangle$ measured with resolution parameters $R = 0.2$, 0.4, and 0.6, respectively, without subtraction of UE (both for data and MC). The right panels of Figs. 17, 18, and 19 display ratios of the model calculations to measured data.

The left panels of Figs. 20, 21, and 22 present the measured p_{T} spectra $F^{p_{\mathrm{T}}}$ and scaled p_{T} spectra F^{z} and F^{ξ} of charged particles in leading charged jets reconstructed with a resolution parameter $R = 0.4$. The UE is not subtracted for both data and MC. The ratios of the calculated MC distributions to measured distributions are shown in the right panels of Figs. 20, 21, and 22.

[1] B. Abbott *et al.* (D0 Collaboration), The Inclusive Jet Cross Section in $p\bar{p}$ Collisions at $\sqrt{s} = 1.8$ TeV, Phys. Rev. Lett. **82**, 2451 (1999).

[2] B. Abbott *et al.* (D0 Collaboration), The Ratio of Jet Cross Sections at $\sqrt{s} = 630$ GeV and 1800 GeV, Phys. Rev. Lett. **86**, 2523 (2001).

[3] V. Abazov *et al.* (D0 Collaboration), Measurement of the Inclusive Jet Cross-Section in $p\bar{p}$ Collisions at $\sqrt{s} = 1.96$ TeV, Phys. Rev. Lett. **101**, 062001 (2008).

[4] F. Abe *et al.* (CDF Collaboration), Inclusive Jet Cross-Section in $\bar{p}p$ Collisions at $\sqrt{s} = 1.8$ TeV, Phys. Rev. Lett. **68**, 1104 (1992).

[5] F. Abe *et al.* (CDF Collaboration), Comparison of Jet Production in $\bar{p}p$ Collisions at $\sqrt{s} = 546$ GeV and 1800 GeV, Phys. Rev. Lett. **70**, 1376 (1993).

[6] F. Abe *et al.* (CDF Collaboration), Inclusive Jet Cross Section in $\bar{p}p$ Collisions at $\sqrt{s} = 1.8$ TeV, Phys. Rev. Lett. **77**, 438 (1996).

[7] T. Affolder *et al.* (CDF Collaboration), Measurement of the inclusive jet cross section in $\bar{p}p$ collisions at $\sqrt{s} = 1.8$ TeV, Phys. Rev. D **64**, 032001 (2001).

[8] A. Abulencia *et al.* (CDF Collaboration), Measurement of the Inclusive Jet Cross Section Using the k_T Algorithm in $p\bar{p}$ Collisions at $\sqrt{s} = 1.96$ TeV, Phys. Rev. Lett. **96**, 122001 (2006).

[9] A. Abulencia *et al.* (CDF Collaboration), Measurement of the inclusive jet cross section in $p\bar{p}$ interactions at $\sqrt{s} = 1.96$ TeV using a cone-based jet algorithm, Phys. Rev. D **74**, 071103 (2006).

[10] A. Abulencia *et al.* (CDF Collaboration), Measurement of the inclusive jet cross section using the k_T algorithm in $p\bar{p}$ collisions at $\sqrt{s} = 1.96$ TeV with the CDF II detector, Phys. Rev. D **75**, 092006 (2007).

[11] T. Aaltonen *et al.* (CDF Collaboration), Measurement of the inclusive jet cross section at the Fermilab Tevatron $p\bar{p}$ collider using a cone-based jet algorithm, Phys. Rev. D **78**, 052006 (2008).

[12] G. Aad *et al.* (ATLAS Collaboration), Properties of jets measured from tracks in proton-proton collisions at center-of-mass energy $\sqrt{s} = 7$ TeV with the ATLAS detector, Phys. Rev. D **84**, 054001 (2011).

[13] S. Chatrchyan *et al.* (CMS Collaboration), Measurement of the Inclusive Jet Cross Section in pp Collisions at $\sqrt{s} = 7$ TeV, Phys. Rev. Lett. **107**, 132001 (2011).

[14] S. Chatrchyan *et al.* (CMS Collaboration), Measurements of differential jet cross sections in proton-proton collisions at $\sqrt{s} = 7$ TeV with the CMS detector, Phys. Rev. D **87**, 112002 (2013).

[15] B. Abelev *et al.* (ALICE Collaboration), Measurement of the inclusive differential jet cross section in pp collisions at $\sqrt{s} = 2.76$ TeV, Phys. Lett. B **722**, 262 (2013).

[16] F. Abe *et al.* (CDF Collaboration), A Measurement of Jet Shapes in $p\bar{p}$ Collisions at $\sqrt{s} = 1.8$ TeV, Phys. Rev. Lett. **70**, 713 (1993).

[17] T. Affolder *et al.* (CDF Collaboration), Charged jet evolution and the underlying event in $p\bar{p}$ collisions at 1.8 TeV, Phys. Rev. D **65**, 092002 (2002).

[18] D. Acosta *et al.* (CDF Collaboration), Study of jet shapes in inclusive jet production in $p\bar{p}$ collisions at $\sqrt{s} = 1.96$ TeV, Phys. Rev. D **71**, 112002 (2005).

[19] S. Abachi *et al.* (D0 Collaboration), Transverse energy distributions within jets in $p\bar{p}$ collisions at $\sqrt{s} = 1.8$ TeV, Phys. Lett. B **357**, 500 (1995).

[20] G. Aad *et al.* (ATLAS Collaboration), Study of jet shapes in inclusive jet production in pp collisions at $\sqrt{s} = 7$ TeV using the ATLAS detector, Phys. Rev. D **83**, 052003 (2011).

[21] S. Chatrchyan *et al.* (CMS Collaboration), Shape, transverse size, and charged hadron multiplicity of jets in pp collisions at 7 TeV, J. High Energy Phys. 06 (2012) 160.

[22] S. Chatrchyan *et al.* (CMS Collaboration), Modification of jet shapes in PbPb collisions at $\sqrt{s_{NN}} = 2.76$ TeV, Phys. Lett. B **730**, 243 (2014).

[23] D. Acosta *et al.* (CDF Collaboration), Momentum distribution of charged particles in jets in dijet events in $p\bar{p}$ collisions at $\sqrt{s} = 1.8$ TeV and comparisons to perturbative QCD predictions, Phys. Rev. D **68**, 012003 (2003).

[24] G. Aad *et al.* (ATLAS Collaboration), Measurement of the jet fragmentation function and transverse profile in proton-proton collisions at a center-of-mass energy of 7 TeV with the ATLAS detector, Eur. Phys. J. C **71**, 1795 (2011).

[25] G. Aad *et al.* (ATLAS Collaboration), Report Nos. ATLAS-CONF-2012-115, ATLAS-COM-CONF-2012-159, https://cds.cern.ch/record/1472936.

[26] S. Chatrchyan *et al.* (CMS Collaboration), Measurement of jet fragmentation into charged particles in pp and PbPb collisions at $\sqrt{s_{NN}} = 2.76$ TeV, J. High Energy Phys. 10 (2012) 087.

[27] T. Sjostrand, S. Mrenna, and P. Z. Skands, PYTHIA 6.4 physics and manual, J. High Energy Phys. 05 (2006) 026.

[28] G. Marchesini, B. R. Webber, G. Abbiendi, I. G. Knowles, M. H. Seymour, and L. Stanco, HERWIG: A Monte Carlo event generator for simulating hadron emission reactions with interfering gluons. Version 5.1—April 1991, Comput. Phys. Commun. **67**, 465 (1992).

[29] G. Corcella, I. G. Knowles, G. Marchesini, S. Moretti, K. Odagiri, P. Richardson, M. H. Seymour, and B. R. Webber, HERWIG 6: An Event generator for hadron emission reactions with interfering gluons (including supersymmetric processes), J. High Energy Phys. 01 (2001) 010.

[30] S. Roesler, R. Engel, and J. Ranft, The Monte Carlo event generator DPMJET-III, in Proc. of Monte Carlo 2000, Lisbon, Portugal, Oct. 2000, arXiv:hep-ph/0012252.

[31] B. Abelev *et al.* (ALICE Collaboration), Measurement of charged jet suppression in Pb-Pb collisions at $\sqrt{s_{NN}} = 2.76$ TeV, J. High Energy Phys. 03 (2014) 013.

[32] J. Beringer *et al.* (Particle Data Group), Review of particle physics (RPP), Phys. Rev. D **86**, 010001 (2012), and 2013 partial update for the 2014 edition.

[33] K. C. Zapp, F. Krauss, and U. A. Wiedemann, A perturbative framework for jet quenching, J. High Energy Phys. 03 (2013) 080.

[34] S. Sapeta and U. A. Wiedemann, Jet hadrochemistry as a characteristics of jet quenching, Eur. Phys. J. C **55**, 293 (2008).

[35] R. Chatterjee, H. Holopainen, T. Renk, and K. J. Eskola, Influence of initial state fluctuations on the production of thermal photons, Nucl. Phys. **A904–A905**, 849c (2013).

[36] K. Aamodt *et al.* (ALICE Collaboration), The ALICE experiment at the CERN LHC, J. Instrum. **3**, S08002 (2008).

[37] B. B. Abelev *et al.* (ALICE), Performance of the ALICE Experiment at the CERN LHC, Int. J. Mod. Phys. A **29**, 1430044 (2014).

[38] J. Alme, Y. Andres, H. Appelshauser, S. Bablok, N. Bialas *et al.*, The ALICE TPC, a large 3-dimensional tracking device with fast readout for ultra-high multiplicity events, Nucl. Instrum. Methods Phys. Res., Sect. A **622**, 316 (2010).

[39] K. Aamodt *et al.* (ALICE Collaboration), Alignment of the ALICE Inner Tracking System with cosmic-ray tracks, J. Instrum. **5**, P03003 (2010).

[40] P. Cortese *et al.* (ALICE Collaboration), ALICE technical design report on forward detectors: FMD, T0 and V0,

Report No. CERN-LHCC-2004-025, https://cds.cern.ch/record/781854 (2004).
[41] B. Abelev *et al.* (ALICE Collaboration), Measurement of inelastic, single- and double-diffraction cross sections in proton–proton collisions at the LHC with ALICE, Eur. Phys. J. C **73**, 2456 (2013).
[42] M. Cacciari, G. P. Salam, and G. Soyez, The anti-k_t jet clustering algorithm, J. High Energy Phys. 04 (2008) 063.
[43] S. Catani, Y. L. Dokshitzer, M. Seymour, and B. Webber, Longitudinally invariant K_t clustering algorithms for hadron hadron collisions, Nucl. Phys. **B406**, 187 (1993).
[44] S. D. Ellis and D. E. Soper, Successive combination jet algorithm for hadron collisions, Phys. Rev. D **48**, 3160 (1993).
[45] M. Cacciari and G. P. Salam, Dispelling the N^3 myth for the k_t jet-finder, Phys. Lett. B **641**, 57 (2006).
[46] G. P. Salam and G. Soyez, A practical seedless infrared-safe cone jet algorithm, J. High Energy Phys. 05 (2007) 086.
[47] B. Ermolaev and V. S. Fadin, Log-log asymptotic form of exclusive cross-sections in quantum chromodynamics, JETP Lett. **33**, 269 (1981).
[48] A. H. Mueller, On the multiplicity of hadrons in QCD jets, Phys. Lett. **104B**, 161 (1981).
[49] P. Z. Skands, Tuning Monte Carlo generators: The Perugia tunes, Phys. Rev. D **82**, 074018 (2010).
[50] R. Brun, F. Carminati, and S. Giani, Report Nos. CERN-W5013, CERN-W-5013, https://cds.cern.ch/record/1082634.
[51] T. Sjostrand and P. Z. Skands, Transverse-momentum-ordered showers and interleaved multiple interactions, Eur. Phys. J. C **39**, 129 (2005).
[52] B. Andersson, G. Gustafson, and B. Soderberg, A general model for jet fragmentation, Z. Phys. C **20**, 317 (1983).
[53] ATLAS Collaboration, Report Nos. ATLAS-CONF-2010-031, ATLAS-COM-CONF-2010-031, https://cds.cern.ch/record/1277665 (2010).
[54] H. L. Lai, J. Huston, S. Kuhlmann, J. Morfin, F. Olness, J. F. Owens, J. Pumplin, and W. K. Tung, Global QCD analysis of parton structure of the nucleon: CTEQ5 parton distributions, Eur. Phys. J. C **12**, 375 (2000).
[55] A. Sherstnev and R. Thorne, Parton distributions for LO generators, Eur. Phys. J. C **55**, 553 (2008).
[56] M. Gluck, E. Reya, and A. Vogt, Dynamical parton distributions of the proton and small x physics, Z. Phys. C **67**, 433 (1995).
[57] G. D'Agostini, A multidimensional unfolding method based on Bayes' theorem, Nucl. Instrum. Methods Phys. Res., Sect. A **362**, 487 (1995).
[58] A. Hocker and V. Kartvelishvili, SVD approach to data unfolding, Nucl. Instrum. Methods Phys. Res., Sect. A **372**, 469 (1996).
[59] T. Adye, Unfolding algorithms and tests using RooUnfold, in Proc. of the PHYSTAT 2011 Workshop, CERN, Geneva, Switzerland, January 2011, Report No. CERN-2011-006, p. 313. See also http://hepunx.rl.ac.uk/~adye/software/unfold/RooUnfold.html.
[60] V. Khachatryan *et al.* (CMS Collaboration), Strange particle production in pp collisions at $\sqrt{s} = 0.9$ and 7 TeV, J. High Energy Phys. 05 (2011) 064.
[61] P. Skands *et al.*, http://mcplots.cern.ch/.
[62] G. Aad *et al.* (ATLAS Collaboration), Measurement of underlying event characteristics using charged particles in pp collisions at $\sqrt{s} = 900$ GeV and 7 TeV with the ATLAS detector, Phys. Rev. D **83**, 112001 (2011).
[63] G. Aad *et al.* (ATLAS Collaboration), Measurements of underlying-event properties using neutral and charged particles in pp collisions at 900 GeV and 7 TeV with the ATLAS detector at the LHC, Eur. Phys. J. C **71**, 1636 (2011).
[64] S. Chatrchyan *et al.* (CMS Collaboration), Measurement of the underlying event activity at the LHC with $\sqrt{s} = 7$ TeV and comparison with $\sqrt{s} = 0.9$ TeV, J. High Energy Phys. 09 (2011) 109.
[65] B. Abelev *et al.* (ALICE Collaboration), Underlying event measurements in pp collisions at $\sqrt{s} = 0.9$ and 7 TeV with the ALICE experiment at the LHC, J. High Energy Phys. 07 (2012) 116.
[66] B. Abelev *et al.* (ALICE Collaboration), Centrality dependence of charged particle production at large transverse momentum in Pb–Pb collisions at $\sqrt{s_{\rm NN}} = 2.76$ TeV, Phys. Lett. B **720**, 52 (2013).
[67] R. Field, and R. C. Group (CDF Collaboration), PYTHIA tune A, HERWIG, and JIMMY in Run 2 at CDF, arXiv:hep-ph/0510198.
[68] B. Abelev *et al.* (ALICE Collaboration), Measurement of inelastic, single- and double-diffraction cross sections in proton–proton collisions at the LHC with ALICE, Eur. Phys. J. C **73**, 2456 (2013).
[69] K. Oyama (ALICE Collaboration), Reference cross section measurements with ALICE in pp and Pb-Pb collisions at LHC, arXiv:1305.7044.
[70] C. Tsallis, Possible generalization of Boltzmann-Gibbs statistics, J. Stat. Phys. **52**, 479 (1988).
[71] C. Tsallis, *Introduction to Nonextensive Statistical Mechanics* (Springer, New York, 2009). For an updated bibliography on this subject, see http://tsallis.cat.cbpf.br/biblio.htm.
[72] B. Abelev *et al.* (ALICE Collaboration), Measurement of charged jet suppression in Pb-Pb collisions at $\sqrt{s_{\rm NN}} = 2.76$ TeV, J. High Energy Phys. 03 (2014) 013.
[73] Y. I. Azimov, Y. L. Dokshitzer, V. A. Khoze, and S. Troyan, Humpbacked QCD Plateau in Hadron Spectra, Z. Phys. C **31**, 213 (1986).

B. Abelev,[71] J. Adam,[37] D. Adamová,[79] M. M. Aggarwal,[83] G. Aglieri Rinella,[34] M. Agnello,[107,90] A. Agostinelli,[26] N. Agrawal,[44] Z. Ahammed,[126] N. Ahmad,[18] I. Ahmed,[15] S. U. Ahn,[64] S. A. Ahn,[64] I. Aimo,[90,107] S. Aiola,[131] M. Ajaz,[15] A. Akindinov,[54] S. N. Alam,[126] D. Aleksandrov,[96] B. Alessandro,[107] D. Alexandre,[98] A. Alici,[101,12] A. Alkin,[3] J. Alme,[35] T. Alt,[39] S. Altinpinar,[17] I. Altsybeev,[125] C. Alves Garcia Prado,[115] C. Andrei,[74] A. Andronic,[93] V. Anguelov,[89] J. Anielski,[50]

T. Antičić,[94] F. Antinori,[104] P. Antonioli,[101] L. Aphecetche,[109] H. Appelshäuser,[49] S. Arcelli,[26] N. Armesto,[16] R. Arnaldi,[107] T. Aronsson,[131] I. C. Arsene,[93,21] M. Arslandok,[49] A. Augustinus,[34] R. Averbeck,[93] T. C. Awes,[80] M. D. Azmi,[85,18] M. Bach,[39] A. Badalà,[103] Y. W. Baek,[66,40] S. Bagnasco,[107] R. Bailhache,[49] R. Bala,[86] A. Baldisseri,[14] F. Baltasar Dos Santos Pedrosa,[34] R. C. Baral,[57] R. Barbera,[27] F. Barile,[31] G. G. Barnaföldi,[130] L. S. Barnby,[98] V. Barret,[66] J. Bartke,[112] M. Basile,[26] N. Bastid,[66] S. Basu,[126] B. Bathen,[50] G. Batigne,[109] A. Batista Camejo,[66] B. Batyunya,[62] P. C. Batzing,[21] C. Baumann,[49] I. G. Bearden,[76] H. Beck,[49] C. Bedda,[90] N. K. Behera,[44] I. Belikov,[51] F. Bellini,[26] R. Bellwied,[117] E. Belmont-Moreno,[60] R. Belmont III,[129] V. Belyaev,[72] G. Bencedi,[130] S. Beole,[25] I. Berceanu,[74] A. Bercuci,[74] Y. Berdnikov,[81,b] D. Berenyi,[130] M. E. Berger,[88] R. A. Bertens,[53] D. Berzano,[25] L. Betev,[34] A. Bhasin,[86] I. R. Bhat,[86] A. K. Bhati,[83] B. Bhattacharjee,[41] J. Bhom,[122] L. Bianchi,[25] N. Bianchi,[68] C. Bianchin,[53] J. Bielčík,[37] J. Bielčíková,[79] A. Bilandzic,[76] S. Bjelogrlic,[53] F. Blanco,[10] D. Blau,[96] C. Blume,[49] F. Bock,[89,70] A. Bogdanov,[72] H. Bøggild,[76] M. Bogolyubsky,[108] F. V. Böhmer,[88] L. Boldizsár,[130] M. Bombara,[38] J. Book,[49] H. Borel,[14] A. Borissov,[92,129] M. Borri,[78] F. Bossú,[61] M. Botje,[77] E. Botta,[25] S. Böttger,[48] P. Braun-Munzinger,[93] M. Bregant,[115] T. Breitner,[48] T. A. Broker,[49] T. A. Browning,[91] M. Broz,[37] E. Bruna,[107] G. E. Bruno,[31] D. Budnikov,[95] H. Buesching,[49] S. Bufalino,[107] P. Buncic,[34] O. Busch,[89] Z. Buthelezi,[61] D. Caffarri,[34,28] X. Cai,[7] H. Caines,[131] L. Calero Diaz,[68] A. Caliva,[53] E. Calvo Villar,[99] P. Camerini,[24] F. Carena,[34] W. Carena,[34] J. Castillo Castellanos,[14] A. J. Castro,[120] E. A. R. Casula,[23] V. Catanescu,[74] C. Cavicchioli,[34] C. Ceballos Sanchez,[9] J. Cepila,[37] P. Cerello,[107] B. Chang,[118] S. Chapeland,[34] J. L. Charvet,[14] S. Chattopadhyay,[126] S. Chattopadhyay,[97] V. Chelnokov,[3] M. Cherney,[82] C. Cheshkov,[124] B. Cheynis,[124] V. Chibante Barroso,[34] D. D. Chinellato,[116,117] P. Chochula,[34] M. Chojnacki,[76] S. Choudhury,[126] P. Christakoglou,[77] C. H. Christensen,[76] P. Christiansen,[32] T. Chujo,[122] S. U. Chung,[92] C. Cicalo,[102] L. Cifarelli,[12,26] F. Cindolo,[101] J. Cleymans,[85] F. Colamaria,[31] D. Colella,[31] A. Collu,[23] M. Colocci,[26] G. Conesa Balbastre,[67] Z. Conesa del Valle,[47] M. E. Connors,[131] J. G. Contreras,[37,11] T. M. Cormier,[129,80] Y. Corrales Morales,[25] P. Cortese,[30] I. Cortés Maldonado,[2] M. R. Cosentino,[115] F. Costa,[34] P. Crochet,[66] R. Cruz Albino,[11] E. Cuautle,[59] L. Cunqueiro,[34,68] A. Dainese,[104] R. Dang,[7] A. Danu,[58] D. Das,[97] I. Das,[47] K. Das,[97] S. Das,[4] A. Dash,[116] S. Dash,[44] S. De,[126] H. Delagrange,[109,a] A. Deloff,[73] E. Dénes,[130] G. D'Erasmo,[31] A. De Caro,[29,12] G. de Cataldo,[100] J. de Cuveland,[39] A. De Falco,[23] D. De Gruttola,[12,29] N. De Marco,[107] S. De Pasquale,[29] R. de Rooij,[53] M. A. Diaz Corchero,[10] T. Dietel,[85,50] P. Dillenseger,[49] R. Divià,[34] D. Di Bari,[31] S. Di Liberto,[105] A. Di Mauro,[34] P. Di Nezza,[68] Ø. Djuvsland,[17] A. Dobrin,[53] T. Dobrowolski,[73] D. Domenicis Gimenez,[115] B. Dönigus,[49] O. Dordic,[21] S. Dørheim,[88] A. K. Dubey,[126] A. Dubla,[53] L. Ducroux,[124] P. Dupieux,[66] A. K. Dutta Majumdar,[97] T. E. Hilden,[42] R. J. Ehlers,[131] D. Elia,[100] H. Engel,[48] B. Erazmus,[109,34] H. A. Erdal,[35] D. Eschweiler,[39] B. Espagnon,[47] M. Esposito,[34] M. Estienne,[109] S. Esumi,[122] D. Evans,[98] S. Evdokimov,[108] D. Fabris,[104] J. Faivre,[67] D. Falchieri,[26] A. Fantoni,[68] M. Fasel,[89,70] D. Fehlker,[17] L. Feldkamp,[50] D. Felea,[58] A. Feliciello,[107] G. Feofilov,[125] J. Ferencei,[79] A. Fernández Téllez,[2] E. G. Ferreiro,[16] A. Ferretti,[25] A. Festanti,[28] J. Figiel,[112] M. A. S. Figueredo,[119] S. Filchagin,[95] D. Finogeev,[52] F. M. Fionda,[31] E. M. Fiore,[31] E. Floratos,[84] M. Floris,[34] S. Foertsch,[61] P. Foka,[93] S. Fokin,[96] E. Fragiacomo,[106] A. Francescon,[28,34] U. Frankenfeld,[93] U. Fuchs,[34] C. Furget,[67] A. Furs,[52] M. Fusco Girard,[29] J. J. Gaardhøje,[76] M. Gagliardi,[25] A. M. Gago,[99] M. Gallio,[25] D. R. Gangadharan,[70,19] P. Ganoti,[80,84] C. Gao,[7] C. Garabatos,[93] E. Garcia-Solis,[13] C. Gargiulo,[34] I. Garishvili,[71] J. Gerhard,[39] M. Germain,[109] A. Gheata,[34] M. Gheata,[34,58] B. Ghidini,[31] P. Ghosh,[126] S. K. Ghosh,[4] P. Gianotti,[68] P. Giubellino,[34] E. Gladysz-Dziadus,[112] P. Glässel,[89] A. Gomez Ramirez,[48] P. González-Zamora,[10] S. Gorbunov,[39] L. Görlich,[112] S. Gotovac,[111] L. K. Graczykowski,[128] A. Grelli,[53] A. Grigoras,[34] C. Grigoras,[34] V. Grigoriev,[72] A. Grigoryan,[1] S. Grigoryan,[62] B. Grinyov,[3] N. Grion,[106] J. F. Grosse-Oetringhaus,[34] J.-Y. Grossiord,[124] R. Grosso,[34] F. Guber,[52] R. Guernane,[67] B. Guerzoni,[26] M. Guilbaud,[124] K. Gulbrandsen,[76] H. Gulkanyan,[1] M. Gumbo,[85] T. Gunji,[121] A. Gupta,[86] R. Gupta,[86] K. H. Khan,[15] R. Haake,[50] Ø. Haaland,[17] C. Hadjidakis,[47] M. Haiduc,[58] H. Hamagaki,[121] G. Hamar,[130] L. D. Hanratty,[98] A. Hansen,[76] J. W. Harris,[131] H. Hartmann,[39] A. Harton,[13] D. Hatzifotiadou,[101] S. Hayashi,[121] S. T. Heckel,[49] M. Heide,[50] H. Helstrup,[35] A. Herghelegiu,[74] G. Herrera Corral,[11] B. A. Hess,[33] K. F. Hetland,[35] B. Hippolyte,[51] J. Hladky,[56] P. Hristov,[34] M. Huang,[17] T. J. Humanic,[19] N. Hussain,[41] T. Hussain,[18] D. Hutter,[39] D. S. Hwang,[20] R. Ilkaev,[95] I. Ilkiv,[73] M. Inaba,[122] G. M. Innocenti,[25] C. Ionita,[34] M. Ippolitov,[96] M. Irfan,[18] M. Ivanov,[93] V. Ivanov,[81] A. Jachołkowski,[27] P. M. Jacobs,[70] C. Jahnke,[115] H. J. Jang,[64] M. A. Janik,[128] P. H. S. Y. Jayarathna,[117] C. Jena,[28] S. Jena,[117] R. T. Jimenez Bustamante,[59] P. G. Jones,[98] H. Jung,[40] A. Jusko,[98] V. Kadyshevskiy,[62] P. Kalinak,[55] A. Kalweit,[34] J. Kamin,[49] J. H. Kang,[132] V. Kaplin,[72] S. Kar,[126] A. Karasu Uysal,[65] O. Karavichev,[52] T. Karavicheva,[52] E. Karpechev,[52] U. Kebschull,[48] R. Keidel,[133] D. L. D. Keijdener,[53] M. Keil SVN,[34] M. M. Khan,[18,c] P. Khan,[97] S. A. Khan,[126] A. Khanzadeev,[81] Y. Kharlov,[108]

B. Kileng,[35] B. Kim,[132] D. W. Kim,[40,64] D. J. Kim,[118] J. S. Kim,[40] M. Kim,[40] M. Kim,[132] S. Kim,[20] T. Kim,[132] S. Kirsch,[39] I. Kisel,[39] S. Kiselev,[54] A. Kisiel,[128] G. Kiss,[130] J. L. Klay,[6] J. Klein,[89] C. Klein-Bösing,[50] A. Kluge,[34] M. L. Knichel,[93] A. G. Knospe,[113] C. Kobdaj,[110,34] M. Kofarago,[34] M. K. Köhler,[93] T. Kollegger,[39] A. Kolojvari,[125] V. Kondratiev,[125] N. Kondratyeva,[72] A. Konevskikh,[52] V. Kovalenko,[125] M. Kowalski,[112] S. Kox,[67] G. Koyithatta Meethaleveedu,[44] J. Kral,[118] I. Králik,[55] A. Kravčáková,[38] M. Krelina,[37] M. Kretz,[39] M. Krivda,[55,98] F. Krizek,[79] E. Kryshen,[34] M. Krzewicki,[93,39] V. Kučera,[79] Y. Kucheriaev,[96,a] T. Kugathasan,[34] C. Kuhn,[51] P. G. Kuijer,[77] I. Kulakov,[49] J. Kumar,[44] P. Kurashvili,[73] A. Kurepin,[52] A. B. Kurepin,[52] A. Kuryakin,[95] S. Kushpil,[79] M. J. Kweon,[89,46] Y. Kwon,[132] P. Ladron de Guevara,[59] C. Lagana Fernandes,[115] I. Lakomov,[47] R. Langoy,[127] C. Lara,[48] A. Lardeux,[109] A. Lattuca,[25] S. L. La Pointe,[107] P. La Rocca,[27] R. Lea,[24] L. Leardini,[89] G. R. Lee,[98] I. Legrand,[34] J. Lehnert,[49] R. C. Lemmon,[78] V. Lenti,[100] E. Leogrande,[53] M. Leoncino,[25] I. León Monzón,[114] P. Lévai,[130] S. Li,[7,66] J. Lien,[127] R. Lietava,[98] S. Lindal,[21] V. Lindenstruth,[39] C. Lippmann,[93] M. A. Lisa,[19] H. M. Ljunggren,[32] D. F. Lodato,[53] P. I. Loenne,[17] V. R. Loggins,[129] V. Loginov,[72] D. Lohner,[89] C. Loizides,[70] X. Lopez,[66] E. López Torres,[9] X.-G. Lu,[89] P. Luettig,[49] M. Lunardon,[28] G. Luparello,[53,24] R. Ma,[131] A. Maevskaya,[52] M. Mager,[34] D. P. Mahapatra,[57] S. M. Mahmood,[21] A. Maire,[51,89] R. D. Majka,[131] M. Malaev,[81] I. Maldonado Cervantes,[59] L. Malinina,[62,d] D. Mal'Kevich,[54] P. Malzacher,[93] A. Mamonov,[95] L. Manceau,[107] V. Manko,[96] F. Manso,[66] V. Manzari,[100] M. Marchisone,[66,25] J. Mareš,[56] G. V. Margagliotti,[24] A. Margotti,[101] A. Marín,[93] C. Markert,[34,113] M. Marquard,[49] I. Martashvili,[120] N. A. Martin,[93] P. Martinengo,[34] M. I. Martínez,[2] G. Martínez García,[109] J. Martin Blanco,[109] Y. Martynov,[3] A. Mas,[109] S. Masciocchi,[93] M. Masera,[25] A. Masoni,[102] L. Massacrier,[109] A. Mastroserio,[31] A. Matyja,[112] C. Mayer,[112] J. Mazer,[120] M. A. Mazzoni,[105] D. Mcdonald,[117] F. Meddi,[22] A. Menchaca-Rocha,[60] E. Meninno,[29] J. Mercado Pérez,[89] M. Meres,[36] Y. Miake,[122] K. Mikhaylov,[54,62] L. Milano,[34] J. Milosevic,[21,e] A. Mischke,[53] A. N. Mishra,[45] D. Miśkowiec,[93] J. Mitra,[126] C. M. Mitu,[58] J. Mlynarz,[129] N. Mohammadi,[53] B. Mohanty,[126,75] L. Molnar,[51] L. Montaño Zetina,[11] E. Montes,[10] M. Morando,[28] D. A. Moreira De Godoy,[109,115] S. Moretto,[28] A. Morreale,[109] A. Morsch,[34] V. Muccifora,[68] E. Mudnic,[111] D. Mühlheim,[50] S. Muhuri,[126] M. Mukherjee,[126] H. Müller,[34] M. G. Munhoz,[115] S. Murray,[85] L. Musa,[34] J. Musinsky,[55] B. K. Nandi,[44] R. Nania,[101] E. Nappi,[100] C. Nattrass,[120] K. Nayak,[75] T. K. Nayak,[126] S. Nazarenko,[95] A. Nedosekin,[54] M. Nicassio,[93] M. Niculescu,[34,58] J. Niedziela,[34] B. S. Nielsen,[76] S. Nikolaev,[96] S. Nikulin,[96] V. Nikulin,[81] B. S. Nilsen,[82] F. Noferini,[12,101] P. Nomokonov,[62] G. Nooren,[53] J. Norman,[119] A. Nyanin,[96] J. Nystrand,[17] H. Oeschler,[89] S. Oh,[131] S. K. Oh,[63,40,f] A. Okatan,[65] T. Okubo,[43] L. Olah,[130] J. Oleniacz,[128] A. C. Oliveira Da Silva,[115] J. Onderwaater,[93] C. Oppedisano,[107] A. Ortiz Velasquez,[32,59] A. Oskarsson,[32] J. Otwinowski,[112,93] K. Oyama,[89] M. Ozdemir,[49] P. Sahoo,[45] Y. Pachmayer,[89] M. Pachr,[37] P. Pagano,[29] G. Paić,[59] C. Pajares,[16] S. K. Pal,[126] A. Palmeri,[103] D. Pant,[44] V. Papikyan,[1] G. S. Pappalardo,[103] P. Pareek,[45] W. J. Park,[93] S. Parmar,[83] A. Passfeld,[50] D. I. Patalakha,[108] V. Paticchio,[100] B. Paul,[97] T. Pawlak,[128] T. Peitzmann,[53] H. Pereira Da Costa,[14] E. Pereira De Oliveira Filho,[115] D. Peresunko,[96] C. E. Pérez Lara,[77] A. Pesci,[101] V. Peskov,[49] Y. Pestov,[5] V. Petráček,[37] M. Petran,[37] M. Petris,[74] M. Petrovici,[74] C. Petta,[27] S. Piano,[106] M. Pikna,[36] P. Pillot,[109] O. Pinazza,[101,34] L. Pinsky,[117] D. B. Piyarathna,[117] M. Płoskoń,[70] M. Planinic,[94,123] J. Pluta,[128] S. Pochybova,[130] P. L. M. Podesta-Lerma,[114] M. G. Poghosyan,[82,34] E. H. O. Pohjoisaho,[42] B. Polichtchouk,[108] N. Poljak,[123,94] A. Pop,[74] S. Porteboeuf-Houssais,[66] J. Porter,[70] B. Potukuchi,[86] S. K. Prasad,[129,4] R. Preghenella,[101,12] F. Prino,[107] C. A. Pruneau,[129] I. Pshenichnov,[52] M. Puccio,[107] G. Puddu,[23] P. Pujahari,[129] V. Punin,[95] J. Putschke,[129] H. Qvigstad,[21] A. Rachevski,[106] S. Raha,[4] S. Rajput,[86] J. Rak,[118] A. Rakotozafindrabe,[14] L. Ramello,[30] R. Raniwala,[87] S. Raniwala,[87] S. S. Räsänen,[42] B. T. Rascanu,[49] D. Rathee,[83] A. W. Rauf,[15] V. Razazi,[23] K. F. Read,[120] J. S. Real,[67] K. Redlich,[73,g] R. J. Reed,[131,129] A. Rehman,[17] P. Reichelt,[49] M. Reicher,[53] F. Reidt,[89,34] R. Renfordt,[49] A. R. Reolon,[68] A. Reshetin,[52] F. Rettig,[39] J.-P. Revol,[34] K. Reygers,[89] V. Riabov,[81] R. A. Ricci,[69] T. Richert,[32] M. Richter,[21] P. Riedler,[34] W. Riegler,[34] F. Riggi,[27] A. Rivetti,[107] E. Rocco,[53] M. Rodríguez Cahuantzi,[2] A. Rodriguez Manso,[77] K. Røed,[21] E. Rogochaya,[62] S. Rohni,[86] D. Rohr,[39] D. Röhrich,[17] R. Romita,[78,119] F. Ronchetti,[68] L. Ronflette,[109] P. Rosnet,[66] A. Rossi,[34] F. Roukoutakis,[84] A. Roy,[45] C. Roy,[51] P. Roy,[97] A. J. Rubio Montero,[10] R. Rui,[24] R. Russo,[25] E. Ryabinkin,[96] Y. Ryabov,[81] A. Rybicki,[112] S. Sadovsky,[108] K. Šafařík,[34] B. Sahlmuller,[49] R. Sahoo,[45] S. Sahoo,[57] P. K. Sahu,[57] J. Saini,[126] S. Sakai,[68] C. A. Salgado,[16] J. Salzwedel,[19] S. Sambyal,[86] V. Samsonov,[81] X. Sanchez Castro,[51] F. J. Sánchez Rodríguez,[114] L. Šándor,[55] A. Sandoval,[60] M. Sano,[122] G. Santagati,[27] D. Sarkar,[126] E. Scapparone,[101] F. Scarlassara,[28] R. P. Scharenberg,[91] C. Schiaua,[74] R. Schicker,[89] C. Schmidt,[93] H. R. Schmidt,[33] S. Schuchmann,[49] J. Schukraft,[34] M. Schulc,[37] T. Schuster,[131] Y. Schutz,[34,109] K. Schwarz,[93] K. Schweda,[93] G. Scioli,[26] E. Scomparin,[107] R. Scott,[120] G. Segato,[28] J. E. Seger,[82] Y. Sekiguchi,[121] I. Selyuzhenkov,[93] K. Senosi,[61] J. Seo,[92] E. Serradilla,[10,60] A. Sevcenco,[58] A. Shabetai,[109] G. Shabratova,[62] R. Shahoyan,[34] A. Shangaraev,[108]

A. Sharma,[86] N. Sharma,[120] S. Sharma,[86] K. Shigaki,[43] K. Shtejer,[9,25] Y. Sibiriak,[96] S. Siddhanta,[102] T. Siemiarczuk,[73] D. Silvermyr,[80] C. Silvestre,[67] G. Simatovic,[123] R. Singaraju,[126] R. Singh,[86] S. Singha,[75,126] V. Singhal,[126] B. C. Sinha,[126] T. Sinha,[97] B. Sitar,[36] M. Sitta,[30] T. B. Skaali,[21] K. Skjerdal,[17] M. Slupecki,[118] N. Smirnov,[131] R. J. M. Snellings,[53] C. Søgaard,[32] R. Soltz,[71] J. Song,[92] M. Song,[132] F. Soramel,[28] S. Sorensen,[120] M. Spacek,[37] E. Spiriti,[68] I. Sputowska,[112] M. Spyropoulou-Stassinaki,[84] B. K. Srivastava,[91] J. Stachel,[89] I. Stan,[58] G. Stefanek,[73] M. Steinpreis,[19] E. Stenlund,[32] G. Steyn,[61] J. H. Stiller,[89] D. Stocco,[109] M. Stolpovskiy,[108] P. Strmen,[36] A. A. P. Suaide,[115] T. Sugitate,[43] C. Suire,[47] M. Suleymanov,[15] R. Sultanov,[54] M. Šumbera,[79] T. J. M. Symons,[70] A. Szabo,[36] A. Szanto de Toledo,[115] I. Szarka,[36] A. Szczepankiewicz,[34] M. Szymanski,[128] J. Takahashi,[116] M. A. Tangaro,[31] J. D. Tapia Takaki,[47,h] A. Tarantola Peloni,[49] A. Tarazona Martinez,[34] M. Tariq,[18] M. G. Tarzila,[74] A. Tauro,[34] G. Tejeda Muñoz,[2] A. Telesca,[34] K. Terasaki,[121] C. Terrevoli,[23] J. Thäder,[93] D. Thomas,[53] R. Tieulent,[124] A. R. Timmins,[117] A. Toia,[49,104] V. Trubnikov,[3] W. H. Trzaska,[118] T. Tsuji,[121] A. Tumkin,[95] R. Turrisi,[104] T. S. Tveter,[21] K. Ullaland,[17] A. Uras,[124] G. L. Usai,[23] M. Vajzer,[79] M. Vala,[55,62] L. Valencia Palomo,[66] S. Vallero,[25,89] P. Vande Vyvre,[34] J. Van Der Maarel,[53] J. W. Van Hoorne,[34] M. van Leeuwen,[53] A. Vargas,[2] M. Vargyas,[118] R. Varma,[44] M. Vasileiou,[84] A. Vasiliev,[96] V. Vechernin,[125] M. Veldhoen,[53] A. Velure,[17] M. Venaruzzo,[69,24] E. Vercellin,[25] S. Vergara Limón,[2] R. Vernet,[8] M. Verweij,[129] L. Vickovic,[111] G. Viesti,[28] J. Viinikainen,[118] Z. Vilakazi,[61] O. Villalobos Baillie,[98] A. Vinogradov,[96] L. Vinogradov,[125] Y. Vinogradov,[95] T. Virgili,[29] V. Vislavicius,[32] Y. P. Viyogi,[126] A. Vodopyanov,[62] M. A. Völkl,[89] K. Voloshin,[54] S. A. Voloshin,[129] G. Volpe,[34] B. von Haller,[34] I. Vorobyev,[125] D. Vranic,[34,93] J. Vrláková,[38] B. Vulpescu,[66] A. Vyushin,[95] B. Wagner,[17] J. Wagner,[93] V. Wagner,[37] M. Wang,[7,109] Y. Wang,[89] D. Watanabe,[122] M. Weber,[117,34] S. G. Weber,[93] J. P. Wessels,[50] U. Westerhoff,[50] J. Wiechula,[33] J. Wikne,[21] M. Wilde,[50] G. Wilk,[73] J. Wilkinson,[89] M. C. S. Williams,[101] B. Windelband,[89] M. Winn,[89] C. G. Yaldo,[129] Y. Yamaguchi,[121] H. Yang,[53] P. Yang,[7] S. Yang,[17] S. Yano,[43] S. Yasnopolskiy,[96] J. Yi,[92] Z. Yin,[7] I.-K. Yoo,[92] I. Yushmanov,[96] A. Zaborowska,[128] V. Zaccolo,[76] A. Zaman,[15] C. Zampolli,[101] S. Zaporozhets,[62] A. Zarochentsev,[125] P. Závada,[56] N. Zaviyalov,[95] H. Zbroszczyk,[128] I. S. Zgura,[58] M. Zhalov,[81] H. Zhang,[7] X. Zhang,[7,70] Y. Zhang,[7] C. Zhao,[21] N. Zhigareva,[54] D. Zhou,[7] F. Zhou,[7] Y. Zhou,[53] Zhuo Zhou,[17] H. Zhu,[7] J. Zhu,[7,109] X. Zhu,[7] A. Zichichi,[12,26] A. Zimmermann,[89] M. B. Zimmermann,[50,34] G. Zinovjev,[3] Y. Zoccarato,[124] and M. Zyzak[49]

(ALICE Collaboration)

[1]*A.I. Alikhanyan National Science Laboratory (Yerevan Physics Institute) Foundation, Yerevan, Armenia*
[2]*Benemérita Universidad Autónoma de Puebla, Puebla, Mexico*
[3]*Bogolyubov Institute for Theoretical Physics, Kiev, Ukraine*
[4]*Bose Institute, Department of Physics and Centre for Astroparticle Physics and Space Science (CAPSS), Kolkata, India*
[5]*Budker Institute for Nuclear Physics, Novosibirsk, Russia*
[6]*California Polytechnic State University, San Luis Obispo, California, USA*
[7]*Central China Normal University, Wuhan, China*
[8]*Centre de Calcul de l'IN2P3, Villeurbanne, France*
[9]*Centro de Aplicaciones Tecnológicas y Desarrollo Nuclear (CEADEN), Havana, Cuba*
[10]*Centro de Investigaciones Energéticas Medioambientales y Tecnológicas (CIEMAT), Madrid, Spain*
[11]*Centro de Investigación y de Estudios Avanzados (CINVESTAV), Mexico City and Mérida, Mexico*
[12]*Centro Fermi-Museo Storico della Fisica e Centro Studi e Ricerche "Enrico Fermi," Rome, Italy*
[13]*Chicago State University, Chicago, Illinois, USA*
[14]*Commissariat à l'Energie Atomique, IRFU, Saclay, France*
[15]*COMSATS Institute of Information Technology (CIIT), Islamabad, Pakistan*
[16]*Departamento de Física de Partículas and IGFAE, Universidad de Santiago de Compostela, Santiago de Compostela, Spain*
[17]*Department of Physics and Technology, University of Bergen, Bergen, Norway*
[18]*Department of Physics, Aligarh Muslim University, Aligarh, India*
[19]*Department of Physics, Ohio State University, Columbus, Ohio, USA*
[20]*Department of Physics, Sejong University, Seoul, South Korea*
[21]*Department of Physics, University of Oslo, Oslo, Norway*
[22]*Dipartimento di Fisica dell'Università 'La Sapienza' and Sezione INFN, Rome, Italy*
[23]*Dipartimento di Fisica dell'Università and Sezione INFN, Cagliari, Italy*
[24]*Dipartimento di Fisica dell'Università and Sezione INFN, Trieste, Italy*
[25]*Dipartimento di Fisica dell'Università and Sezione INFN, Turin, Italy*

[26]Dipartimento di Fisica e Astronomia dell'Università and Sezione INFN, Bologna, Italy
[27]Dipartimento di Fisica e Astronomia dell'Università and Sezione INFN, Catania, Italy
[28]Dipartimento di Fisica e Astronomia dell'Università and Sezione INFN, Padova, Italy
[29]Dipartimento di Fisica 'E.R. Caianiello' dell'Università and Gruppo Collegato INFN, Salerno, Italy
[30]Dipartimento di Scienze e Innovazione Tecnologica dell'Università del Piemonte Orientale and Gruppo Collegato INFN, Alessandria, Italy
[31]Dipartimento Interateneo di Fisica 'M. Merlin' and Sezione INFN, Bari, Italy
[32]Division of Experimental High Energy Physics, University of Lund, Lund, Sweden
[33]Eberhard Karls Universität Tübingen, Tübingen, Germany
[34]European Organization for Nuclear Research (CERN), Geneva, Switzerland
[35]Faculty of Engineering, Bergen University College, Bergen, Norway
[36]Faculty of Mathematics, Physics and Informatics, Comenius University, Bratislava, Slovakia
[37]Faculty of Nuclear Sciences and Physical Engineering, Czech Technical University in Prague, Prague, Czech Republic
[38]Faculty of Science, P.J. Šafárik University, Košice, Slovakia
[39]Frankfurt Institute for Advanced Studies, Johann Wolfgang Goethe-Universität Frankfurt, Frankfurt, Germany
[40]Gangneung-Wonju National University, Gangneung, South Korea
[41]Gauhati University, Department of Physics, Guwahati, India
[42]Helsinki Institute of Physics (HIP), Helsinki, Finland
[43]Hiroshima University, Hiroshima, Japan
[44]Indian Institute of Technology Bombay (IIT), Mumbai, India
[45]Indian Institute of Technology Indore, Indore (IITI), India
[46]Inha University, Incheon, South Korea
[47]Institut de Physique Nucléaire d'Orsay (IPNO), Université Paris-Sud, CNRS-IN2P3, Orsay, France
[48]Institut für Informatik, Johann Wolfgang Goethe-Universität Frankfurt, Frankfurt, Germany
[49]Institut für Kernphysik, Johann Wolfgang Goethe-Universität Frankfurt, Frankfurt, Germany
[50]Institut für Kernphysik, Westfälische Wilhelms-Universität Münster, Münster, Germany
[51]Institut Pluridisciplinaire Hubert Curien (IPHC), Université de Strasbourg, CNRS-IN2P3, Strasbourg, France
[52]Institute for Nuclear Research, Academy of Sciences, Moscow, Russia
[53]Institute for Subatomic Physics of Utrecht University, Utrecht, Netherlands
[54]Institute for Theoretical and Experimental Physics, Moscow, Russia
[55]Institute of Experimental Physics, Slovak Academy of Sciences, Košice, Slovakia
[56]Institute of Physics, Academy of Sciences of the Czech Republic, Prague, Czech Republic
[57]Institute of Physics, Bhubaneswar, India
[58]Institute of Space Science (ISS), Bucharest, Romania
[59]Instituto de Ciencias Nucleares, Universidad Nacional Autónoma de México, Mexico City, Mexico
[60]Instituto de Física, Universidad Nacional Autónoma de México, Mexico City, Mexico
[61]iThemba LABS, National Research Foundation, Somerset West, South Africa
[62]Joint Institute for Nuclear Research (JINR), Dubna, Russia
[63]Konkuk University, Seoul, South Korea
[64]Korea Institute of Science and Technology Information, Daejeon, South Korea
[65]KTO Karatay University, Konya, Turkey
[66]Laboratoire de Physique Corpusculaire (LPC), Clermont Université, Université Blaise Pascal, CNRS–IN2P3, Clermont-Ferrand, France
[67]Laboratoire de Physique Subatomique et de Cosmologie, Université Grenoble-Alpes, CNRS-IN2P3, Grenoble, France
[68]Laboratori Nazionali di Frascati, INFN, Frascati, Italy
[69]Laboratori Nazionali di Legnaro, INFN, Legnaro, Italy
[70]Lawrence Berkeley National Laboratory, Berkeley, California, USA
[71]Lawrence Livermore National Laboratory, Livermore, California, USA
[72]Moscow Engineering Physics Institute, Moscow, Russia
[73]National Centre for Nuclear Studies, Warsaw, Poland
[74]National Institute for Physics and Nuclear Engineering, Bucharest, Romania
[75]National Institute of Science Education and Research, Bhubaneswar, India
[76]Niels Bohr Institute, University of Copenhagen, Copenhagen, Denmark
[77]Nikhef, National Institute for Subatomic Physics, Amsterdam, Netherlands
[78]Nuclear Physics Group, STFC Daresbury Laboratory, Daresbury, United Kingdom
[79]Nuclear Physics Institute, Academy of Sciences of the Czech Republic, Řež u Prahy, Czech Republic

[80]*Oak Ridge National Laboratory, Oak Ridge, Tennessee, USA*
[81]*Petersburg Nuclear Physics Institute, Gatchina, Russia*
[82]*Physics Department, Creighton University, Omaha, Nebraska, USA*
[83]*Physics Department, Panjab University, Chandigarh, India*
[84]*Physics Department, University of Athens, Athens, Greece*
[85]*Physics Department, University of Cape Town, Cape Town, South Africa*
[86]*Physics Department, University of Jammu, Jammu, India*
[87]*Physics Department, University of Rajasthan, Jaipur, India*
[88]*Physik Department, Technische Universität München, Munich, Germany*
[89]*Physikalisches Institut, Ruprecht-Karls-Universität Heidelberg, Heidelberg, Germany*
[90]*Politecnico di Torino, Turin, Italy*
[91]*Purdue University, West Lafayette, Indiana, USA*
[92]*Pusan National University, Pusan, South Korea*
[93]*Research Division and ExtreMe Matter Institute EMMI, GSI Helmholtzzentrum für Schwerionenforschung, Darmstadt, Germany*
[94]*Rudjer Bošković Institute, Zagreb, Croatia*
[95]*Russian Federal Nuclear Center (VNIIEF), Sarov, Russia*
[96]*Russian Research Centre Kurchatov Institute, Moscow, Russia*
[97]*Saha Institute of Nuclear Physics, Kolkata, India*
[98]*School of Physics and Astronomy, University of Birmingham, Birmingham, United Kingdom*
[99]*Sección Física, Departamento de Ciencias, Pontificia Universidad Católica del Perú, Lima, Peru*
[100]*Sezione INFN, Bari, Italy*
[101]*Sezione INFN, Bologna, Italy*
[102]*Sezione INFN, Cagliari, Italy*
[103]*Sezione INFN, Catania, Italy*
[104]*Sezione INFN, Padova, Italy*
[105]*Sezione INFN, Rome, Italy*
[106]*Sezione INFN, Trieste, Italy*
[107]*Sezione INFN, Turin, Italy*
[108]*SSC IHEP of NRC Kurchatov institute, Protvino, Russia*
[109]*SUBATECH, Ecole des Mines de Nantes, Université de Nantes, CNRS-IN2P3, Nantes, France*
[110]*Suranaree University of Technology, Nakhon Ratchasima, Thailand*
[111]*Technical University of Split FESB, Split, Croatia*
[112]*The Henryk Niewodniczanski Institute of Nuclear Physics, Polish Academy of Sciences, Cracow, Poland*
[113]*The University of Texas at Austin, Physics Department, Austin, Texas, USA*
[114]*Universidad Autónoma de Sinaloa, Culiacán, Mexico*
[115]*Universidade de São Paulo (USP), São Paulo, Brazil*
[116]*Universidade Estadual de Campinas (UNICAMP), Campinas, Brazil*
[117]*University of Houston, Houston, Texas, USA*
[118]*University of Jyväskylä, Jyväskylä, Finland*
[119]*University of Liverpool, Liverpool, United Kingdom*
[120]*University of Tennessee, Knoxville, Tennessee, USA*
[121]*University of Tokyo, Tokyo, Japan*
[122]*University of Tsukuba, Tsukuba, Japan*
[123]*University of Zagreb, Zagreb, Croatia*
[124]*Université de Lyon, Université Lyon 1, CNRS/IN2P3, IPN-Lyon, Villeurbanne, France*
[125]*V. Fock Institute for Physics, St. Petersburg State University, St. Petersburg, Russia*
[126]*Variable Energy Cyclotron Centre, Kolkata, India*
[127]*Vestfold University College, Tonsberg, Norway*
[128]*Warsaw University of Technology, Warsaw, Poland*
[129]*Wayne State University, Detroit, Michigan, USA*
[130]*Wigner Research Centre for Physics, Hungarian Academy of Sciences, Budapest, Hungary*
[131]*Yale University, New Haven, Connecticut, USA*
[132]*Yonsei University, Seoul, South Korea*
[133]*Zentrum für Technologietransfer und Telekommunikation (ZTT), Fachhochschule Worms, Worms, Germany*

[a]Deceased
[b]Also at St. Petersburg State Polytechnical University.
[c]Also at Department of Applied Physics, Aligarh Muslim University, Aligarh, India.

[d]Also at M.V. Lomonosov Moscow State University, D.V. Skobeltsyn Institute of Nuclear Physics, Moscow, Russia.
[e]Also at University of Belgrade, Faculty of Physics and "Vinča" Institute of Nuclear Sciences, Belgrade, Serbia.
[f]Permanent Address: Konkuk University, Seoul, Korea.
[g]Also at Institute of Theoretical Physics, University of Wroclaw, Wroclaw, Poland.
[h]Also at University of Kansas, Lawrence, Kansas, USA.